Journal of Asian Earth Sciences 190 (2020) 104180

Contents lists available at ScienceDirect

Journal of Asian Earth Sciences

journal homepage: www.elsevier.com/locate/jseaes

# Late Mesozoic oxidized magma for porphyry Ag mineralization: A comparative study from mineralized and barren granite porphyries in the Lengshuikeng Ag-(Pb-Zn) deposit, South China

Youqiang Qi[a,*], Ruizhong Hu[a], Jianfeng Gao[a], Chengbiao Leng[b], Haotian Gong[a,c], Wei Gao[a]

[a] State Key Laboratory of Ore Deposit Geochemistry, Institute of Geochemistry, Chinese Academy of Sciences, Guiyang 550081, PR China
[b] State Key Laboratory of Nuclear Resources and Environment, East China University of Technology, Nanchang 330013, PR China
[c] University of Chinese Academy of Sciences, Beijing 100049, PR China

ARTICLE INFO

*Keywords:*
Granite porphyry
Petrogenesis
Magmatic oxidizing hydrous conditions
Porphyry silver deposit
Lengshuikeng deposit

ABSTRACT

The Lengshuikeng Ag-(Pb-Zn) deposit (LSKD) is one of the largest independent porphyry silver deposits in China. Its silver mineralization is related to the Late Mesozoic granite porphyry, but the oxidizing hydrous conditions of the associated magma are still unclear. This study focuses on the associated granite porphyry (GP) and barren K-feldspar granite porphyry (KFGP) to constrain their oxidizing hydrous conditions. New zircon U-Pb dating shows the GP emplaced at 155.8 ± 1.9 Ma and 158.5 ± 2.3 Ma for GP, and the KFGP emplaced at 136.6 ± 1.9 Ma. Both granites are peraluminous with A/CNK ratios of 1.09–3.01 (mean = 1.48), similar to that of typical S-type granites. They are enriched in light rare earth elements (LREE), with large $(La/Yb)_N$ (7.0–19.1 for the GP and 1.8–34.3 for the KFGP) and negative Eu anomalies (0.29–0.67 for the GP and 0.02–0.05 for the KFGP). The GP has $\varepsilon_{Nd}(t)$ values ranging from − 10.0 to − 9.7 with $T_{DM2}$ ages of 1688–1915 Ma, while the KFGP has higher $\varepsilon_{Nd}(t)$ values ranging from − 7.5 to − 7.6 with younger $T_{DM2}$ ages of 1538–1548 Ma. The initial Pb isotopic ratios for $(^{206}Pb/^{204}Pb)_i$, $(^{207}Pb/^{204}Pb)_i$ and $(^{208}Pb/^{204}Pb)_i$ are 17.647–17.952, 15.555–15.604 and 37.851–38.541, respectively. Our new chemical and isotopic data suggest that both granites were dominantly derived from dehydration melting of the Proterozoic meta-sedimentary rocks, with more dehydration fluids for the GP and relatively more mantle contribution to the KFGP. Both granites underwent fractional crystallization of plagioclase, K-feldspar and ilmenite/magnetite followed by minor assimilation of the upper crust. Comparative study on the relative water content, oxidation state and melting temperature of magma have shown relatively moderate oxidation state and water content in the associated magma probably played more important roles in porphyry silver mineralization than other factors in porphyry Cu deposit. This study helps deepen the understanding of silver mineralization.

## 1. Introduction

Silver often occurs with other metals, such as Cu and Au, in hydrothermal deposits. The styles of silver hydrothermal mineralization can vary from veins, skarn, greisen to porphyry type. Increasing giant independent silver deposits as a general porphyry type or a special epithermal type (unified as porphyry type below), such as Pachuca (45,000 t. Ag) and Fresnillo (16,050 t. Ag) in Mexico and El Indio (3100 t Ag) in Chile, have attracted great attention due to their high grades and large tonnages (Simmons et al., 2005). The porphyry Ag ore bodies are usually far away from the central granite porphyry. This leads to the difficulty to identify ore-related granite porphyry and insufficient research on their mineralization fertility. Most researchers suggest the silver mineralization is related to magmatic-hydrothermal activities of intermediate-felsic magma (e.g. Megaw et al., 1988). The metal and sulfur of porphyry copper mineralization have been thought to be magmatic origin (Cline and Bodnar, 1991; Hedenquist and Lowenstern, 1994; Candela and Piccoli, 2005; Halter et al., 2005; Williams-Jones and Heinrich, 2005; Zajacz et al., 2008), but the nature of silver–mineralization-related magma remains unclear.

Previous studies have shown granites related to porphyry Cu deposit generally have relatively high $fO_2$ ($fO_2$ > ΔFMQ + 2 or ΔNNO + 1) and water contents as the precondition for the formation of copper-rich metallogenic magma (Mungall, 2002; Jugo, 2009; Richards, 2003, 2009; Griffin et al., 2013; Hou et al., 2015, 2017; Sun et al., 2017). Similar to copper, silver is an incompatible chalcophile element, and its

* Corresponding authors.
*E-mail address:* qiyouqiang@sina.com (Y. Qi).

https://doi.org/10.1016/j.jseaes.2019.104180
Received 30 June 2019; Received in revised form 22 November 2019; Accepted 1 December 2019
Available online 06 December 2019
1367-9120/ 

behavior is also strongly controlled by sulfides. The speciation of sulfur is controlled by oxygen fugacity. Hence, it is speculated that a relatively high oxygen fugacity is a necessary condition for making a silver deposit. In addition, more water content in magma source will promote the differentiation of magma and the formation of ore-forming fluid (Richards, 2011; Wang et al., 2014b,c). However, the $fO_2$ and water content of the granite porphyry related to porphyry Ag deposit has not been well constrained.

The Lengshuikeng Ag-(Pb-Zn) deposit (LSKD), with an ore reserves of ~43 Mt and average grades of 204.53 g/t Ag, 2.11% Pb and 2.61% Zn, is one of the largest independent porphyry silver deposits in China (Wang et al., 2014a). Based on the alteration zoning characteristics, consistency of mineralization and magmatic crystallization chronology, the silver mineralization is closely related to the granite porphyry occurred in the LSKD (Wang et al., 2014a; Meng et al., 2007, 2012). This study focuses on the mineralized granite porphyry and barren granite in the LSKD, and compares their magma sources, formation, evolution, oxygen fugacity, and water content, to clarify the controlling factors on silver mineralization. This study also helps us deepen the current understanding of silver mineralization.

## 2. Regional geology

The Lengshuikeng Ag-Pb-Zn deposit locates in the north part of the Wuyi metallogenic belt (Ye, 1987; Liu et al., 1994; Yang et al., 2004; Meng et al., 2007; Wang et al., 2010), and on the southern side of the Gan-Hang Tectonic Belt (GHTB), which is the northeastern boundary between the Yangtze and Cathaysia blocks (Fig. 1, Li et al. 2011; Wong et al. 2011). In the North Wuyi Area (NWA), the Dongxiang, Tianhuashan, Huangangshan, and Lizikeng (Tongboshan) Basins distribute along the regional EW-trending basement uplift, represented by a prominent series of NNE-trending volcanic basins (Fig. 1b). Many ore deposits developed within these volcanic basins, such as the Lengshuikeng Ag-Pb-Zn deposit, Xiongjiashan Mo deposit, Shengmikeng Pb-Zn deposit, Jiaotang Pb-Zn deposit and Jinzhuping Mo deposit (Fig. 1; Luo et al., 2009; Su et al., 2013), all of which are related to the Late Mesozoic magmatism (Liu et al., 1994; Meng et al., 2007; Wang et al., 2010; Yang et al., 2004; Ye, 1987).

The NWA has undergone a long and complex geodynamic evolution from Proterozoic to Mesozoic (Yu et al., 2009), including the Neoproterozoic continental amalgamation between the Yangtze and Cathaysia blocks (WX, Li et al., 2008); the Kwangsian tectonothermal events that are synchronous with the Early Paleozoic orogeny in South China (ZX, Li et al., 2010; Yu et al., 2012); and the Indosinian (Late Permian to Triassic) and Yanshanian (Jurassic to Cretaceous) tectonothermal events (Lu et al., 2007; Mei, 1998; Yu et al., 2012; Wang et al., 2013b). Pre-Sinian basement rocks, Sinian to Middle Triassic marine sedimentary strata, Mesozoic–Cenozoic terrestrial sequence and volcanic rocks comprise the stratigraphic system in the NWA. Several unconformities between different structural layers exist within the system. The lower member of the basement is a set of metamorphic rocks formed between Late Archean and Early Proterozoic, whereas the upper part of the basement consists of Late Meso-Neoproterozoic metamorphic strata that were originally marine volcanic–sedimentary formations (Zhao, 1999). The lower members of the covering strata include the Lower Sinian to Lower Paleozoic continuous sedimentary rocks with low-grade metamorphic flyschoid formations. The upper member of the covering rocks consists of Devonian–Middle Triassic strata. The Late Triassic–Cretaceous strata are widely and continuously distributed in the NWA. They are dominated by continental sedimentary and volcanic

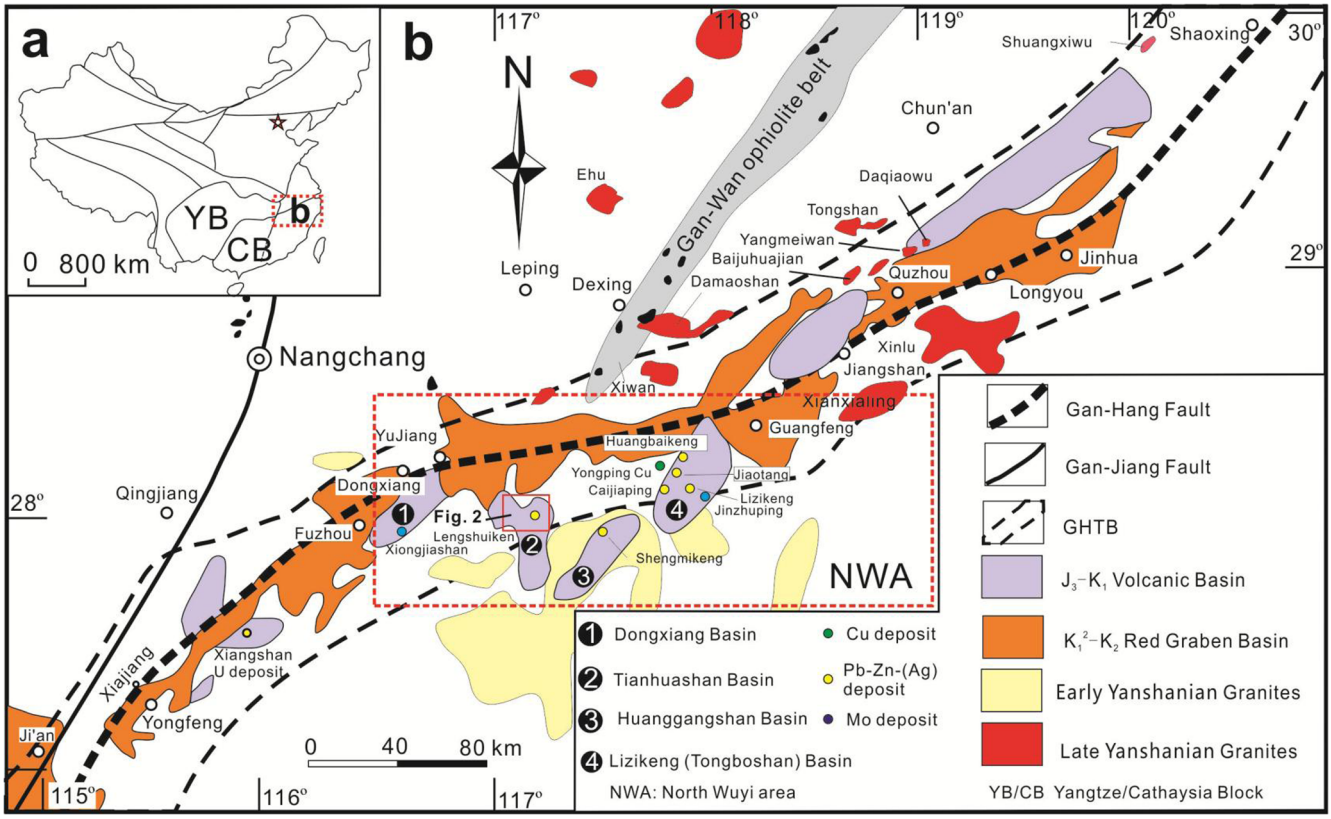


**Fig. 1.** (a) Simplified map of China; (b) Geological map of the Gan–Hang tectonic belt (GHTB), and volcanic basins in the North Wuyi Area (NWA), South China (modified from Qi et al., 2016).

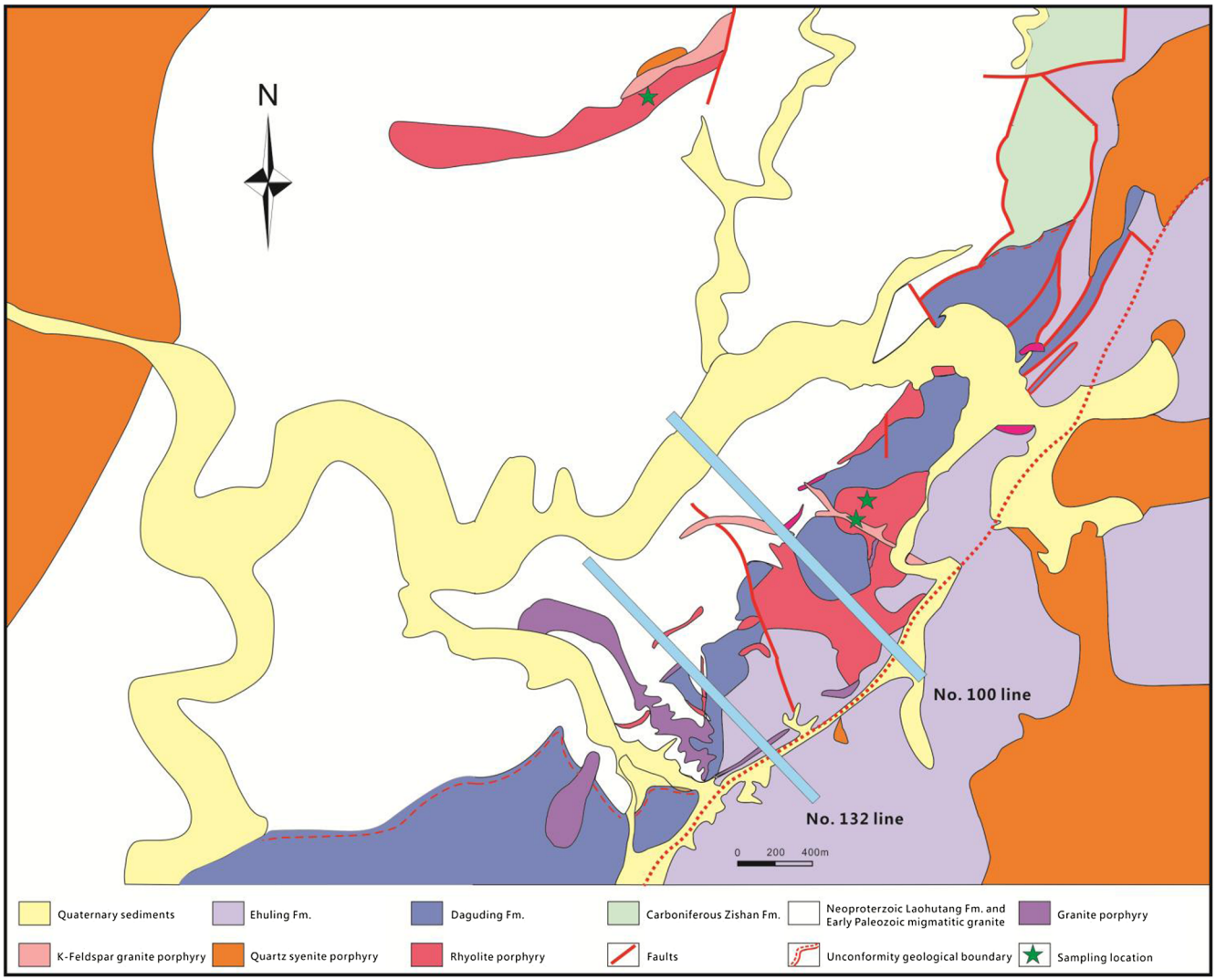


**Fig. 2.** Geological map of the Lengshuikeng Ag-(Pb-Zn) deposit (LSKD).

rocks, substantially varying in longitudinal and landscape orientations (JXBGMR (Bureau of Geology and Mineral Resources of Jiangxi Province), 1984; JXBGMR (Department of Geology and Mineral Resources of Jiangxi Province), 1997; Liu et al., 1994; Mei, 1998; Xie et al., 2006).

## 3. Deposit geology

The stratigraphic sequence in the Lengshuikeng Ag-(Pb-Zn) deposit contains the Jurassic Daguding and E'huling Formations (Meng et al., 2007). The Daguding Formation occurring in the middle part is comprised of andesite and rhyolitic tuffs and tuffaceous siltstone, and the E'huling Formation outcropping continuously in the northeast consists of tuffs, rhyolite, tuffaceous siltstone, sandstone, and manganese- and iron-rich carbonates. The prominent structural features in the LSKD are NE-striking reverse faults dipping toward NW, including $F_1$ and $F_2$ (Fig. 2). The $F_1$ fault was formed before the eruption and sedimentation of the E'huling and Daguding formations, whereas the $F_2$ fault may have been initiated during and continued after their eruption and sedimentation (Wang et al., 2014a). The footwall of $F_2$ fault displays a normal stratigraphic sequence of E'huling ($J_3e$) and Daguding ($J_3d$), whereas its hanging wall exhibits a sequence of Sinian rocks (Laohutang Formation, $Z_2l$) (Fig. 2). The $F_2$ fault is the most important rock- and ore-controlling structure in the LSKD. The Jurassic granite porphyry intruded along the $F_2$ fault, and the occurrence of lead, zinc and silver ore bodies are also controlled by $F_2$ fault (Qi et al., 2015).

The magmatism in the LSKD mainly developed in the Early Paleozoic, Late Jurassic and Early Cretaceous. The Early Paleozoic igneous rocks comprise of pegmatite and migmatitic granite prior to the metal mineralization. The Jurassic igneous rocks are mainly hypabyssal granite porphyry including the Yinluling and Yinzhushan porphyries related to the Ag-Pb-Zn mineralization. The Early Cretaceous rocks include quartz syenite porphyry, rhyolite porphyry and K-feldspar granite porphyry (Fig. 2). Previous studies have reported that rhyolite porphyry and K-feldspar granite porphyry cut the granite porphyry and pyroclastic carbonate ore-hosted rocks as well as the quartz syenite porphyry (Meng et al., 2007). SHRIMP and LA-ICP-MS zircon U-Pb dating has identified the ages for the granite porphyry (155 Ma, 157 Ma, and 162 Ma), K-feldspar granite porphyry (140 Ma), quartz syenite porphyry (139 Ma and 144 Ma) and rhyolite porphyry (140 Ma) (Meng et al., 2012; Qiu et al., 2013; Su et al., 2013; Wang et al., 2013a; Yu et al., 2012).

Two types of mineralization have been identified in the LSKD. One type is vein-veinlet-disseminated Ag-Pb-Zn-Cu-Au mineralization which is mainly developed in the Yinluling porphyry and its periphery. The ore bodies mainly occur in the major body of porphyry granite, with the

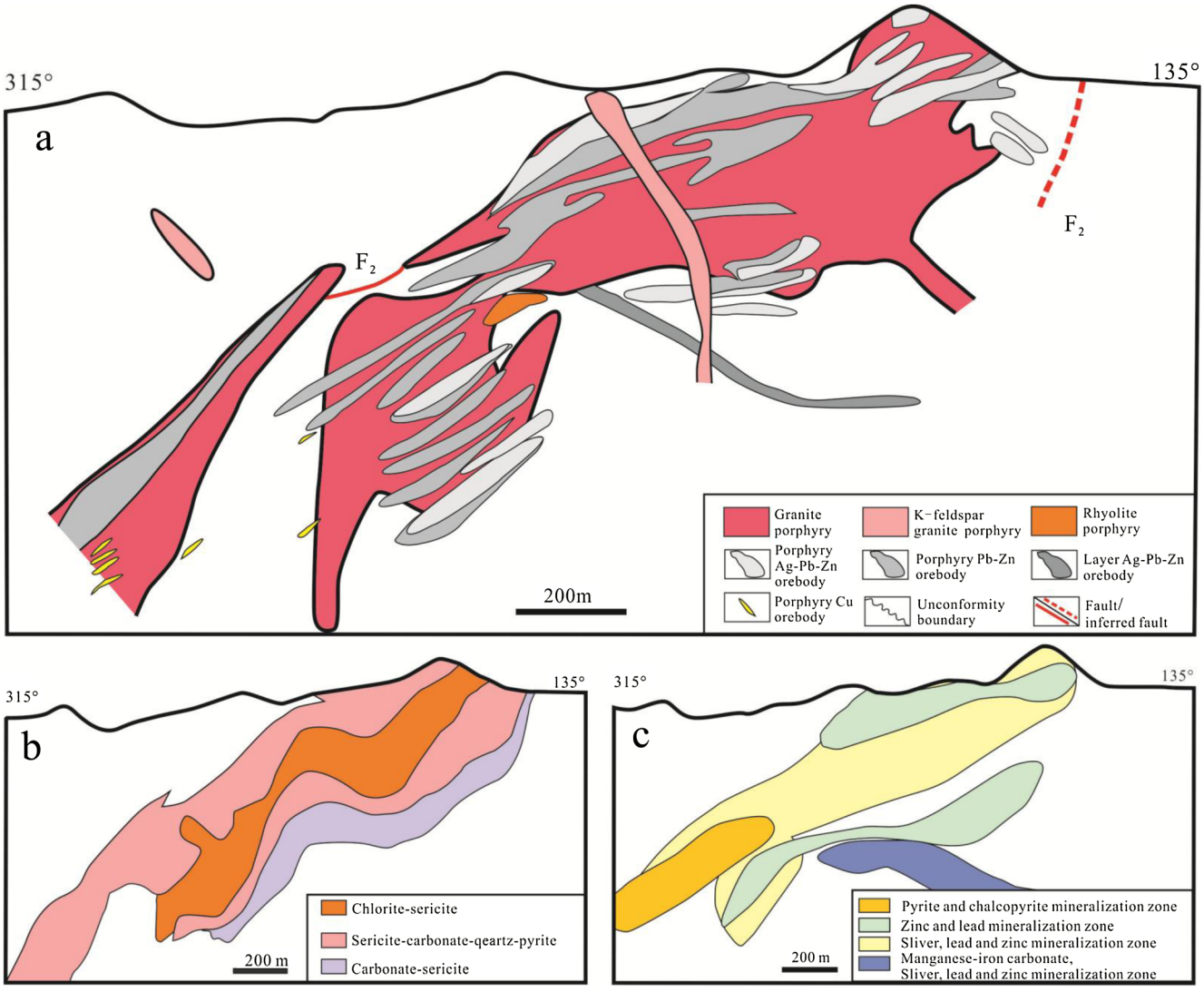


**Fig. 3.** (a) Geological features; (b) alteration zoning; and (c) mineralization zoning along No. 100 section in the LSKD.

inner zone in contact between the granite porphyry and country rocks. The other type is massive Ag-Pb-Zn-Fe-Mn mineralization sandwiched in layered volcanic clastic rocks of the Daguding Formation. This type of mineralization is generally under the first type ore body (Fig. 3). In general, the spatial distribution of ore bodies in porphyry is related to alteration and superposition. The Cu-rich ore body is closely associated with chlorite and sericite alteration in the inner zone of porphyry granite, while the Pb-Zn-Ag ore body is hosted in sericitization, carbonatization and silicification zone. The Ag-Pb-Zn ore body with carbonatization and sericitization situates in the outer peripheral (or distal) zone (Fig. 3). Although the occurrence, mineral constituents, and the zoning of alteration assemblages of both mineralization types are distinct from each other, they are considered to have resulted from the same mineralization system closely related to magmatic-hydrothermal fluids of granite porphyry (Qi et al., 2015; Leng and Qi, 2018). The major ore minerals of the LSKD include sphalerite, galena, pyrite and various silver minerals. The dominant silver minerals are acanthite ($Ag_2S$) and native silver, which occur in fissures within manganese–iron carbonate or in the intergranular space between manganese–iron carbonate and early sulfides (Lu et al., 2012).

## 4. Samples and analytical methods

### 4.1. Samples

#### 4.1.1. Granite porphyry (GP)

The granite porphyry outcrops in two places, with one hosting the main ore-body and the other in the northwest part of the LSKD (Fig. 2), where both plutons exhibit porphyritic texture (Fig. 4). The phenocrysts are mainly quartz and K-feldspar (about 15–35% in volume) with grains of 0.5–10 mm, whereas the groundmass is fine-grained (0.01–0.07 mm). Rock-forming minerals include quartz (37–65%), K-feldspar (21–49%), plagioclase (7–13%), and minor biotite (< 1–2%). Accessory minerals are mainly zircon and apatite. Four GP samples were collected in the northwest part of the mining area, and another sixteen samples of GP were collected in Yinzhushan.

#### 4.1.2. K-feldspar granite porphyry (KFGP)

The K-feldspar granite porphyry intrusion outcrops in Yinzhushan (Fig. 2) and is pinkish with porphyritic texture (Fig. 4). The phenocrysts (about 5–8%) are euhedral grains of K-feldspar and quartz, whereas the

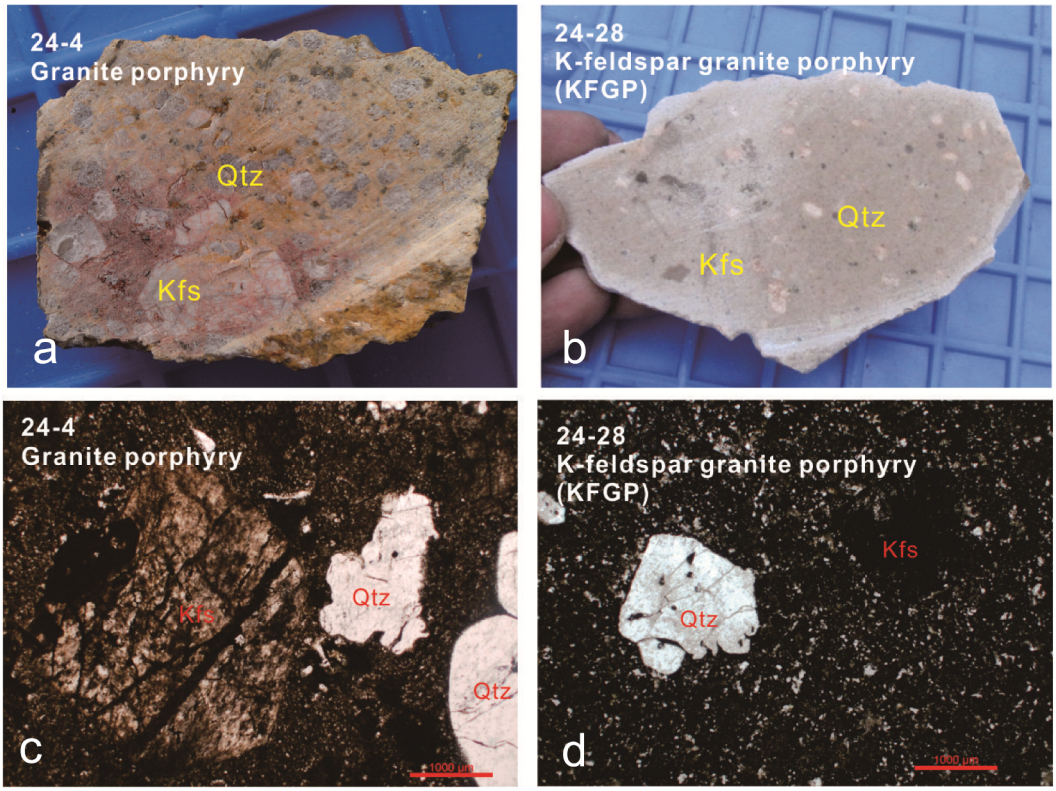


**Fig. 4.** Photographs and photomicrographs of representative specimens from the granite porphyry (GP) and the K-feldspar granite porphyry (KFGP) in the LSKD. Kfs: k-feldspar; Qtz: quartz.

groundmass shows a fine-grained texture consisting of K-feldspar, quartz and minor biotite. Previous studies yielded a LA-ICP-MS zircon U-Pb ages of 138.6 Ma and 140 Ma, respectively (Su et al., 2014; Wang et al., 2013a). In this study, seven KFGP samples were collected for analysis.

### 4.2. Analytical methods

Zircons were extracted from samples using conventional heavy liquid and magnetic techniques. Representative zircon grains were handpicked under a binocular microscope and mounted in an epoxy resin mount, and then polished and coated with a gold film, which was documented with transmitted and reflected light micrographs as well as cathodoluminescence (CL) images to reveal their internal structures. The CL images were obtained using LEO1450VP scanning electron microscope at the Institute of Geology and Geophysics, Chinese Academy of Sciences (IGGCAS), Beijing. The zircon U-Pb isotopic analyses and U, Th and Pb concentrations were also determined in IGGCAS, using the Cameca IMS-1280 SIMS. The analytical procedures are the same as those described by Li et al. (2009). The analytical pits were about 20 × 30 μm in size and ellipsoidal in shape. Pb/U calibration was performed relative to standard zircon 91500 with U and Th concentrations of ca. 81 and 29 ppm, respectively (Wiedenbeck et al., 1995). Analyses of the standard zircon Plésovice were carried out after every 3–4 unknown analyses. U–Th–Pb ratios was calibrated against measured rations of standard zircon Plésovice with an age of 337 Ma (Sláma et al., 2008). Measured compositions were corrected for common Pb using the measured non-radiogenic $^{204}$Pb. Uncertainties on individual analyses are reported at 1SD level, and the ages for pooled U-Pb analyses are quoted with 2SD. Data reduction was carried out using the Isoplot/Ex v.4.15 program of Ludwig (2008). In order to monitor the external uncertainties of SIMS U–Pb measurements calibrated against Plésovice standard, Qinghu zircon standard was alternately analyzed as an unknown together with the unknown zircons. A total of 8 measurements were onducted on Qinghu zircon, and the Concordia Age of 160.3 ± 1.7 Ma (2SD) is identical within error with the recommended value of 159.2 ± 0.2 Ma (2SD) (Li et al., 2013a,b).

Zircon U-Pb dating and trace element analyses were simultaneously by LA-ICP-MS at the State Key Laboratory of Ore Deposit Geochemistry, Institute of Geochemistry Chinese Academy of Sciences (SKLODG, IGCAS), Guiyang. Laser ablation was performed using a RESOlution 193 nm ArF excimer laser. An Agilent 7900 ICP-MS instrument was used to acquire ion-signal intensities. Helium was applied as a carrier gas which was mixed with Argon via a T-connector before entering the ICP-MS. Each analysis incorporated a background acquisition of approximately 30 s (gas blank) followed by 60 s of data acquisition from the sample. Off-line data processing selection and integration of background and analytical signals, time-drift correction and quantitative calibration for trace element analyses and U-Pb dating were performed by ICPMSDataCal (Liu et al., 2010). zircon 91500 was used as the external standard for U-Pb dating and analyzed twice every 6–8 analyses. Uncertainty of preferred values for the external standard 91500 was propagated to the ultimate results of the samples. Concordia diagrams and weighted mean age calculations were made using Isoplot (Ludwig, 2008). Trace element compositions of zircons were calibrated against multiple-reference materials (NIST 610) combined with Si internal standardization. The preferred values of element concentrations for the USGS reference glasses are from the GeoReM database (http://georem.mpch-mainz.gwdg.de/).

Major elements of whole rocks were analyzed using the Axios PW4400 X-ray fluorescence spectrometer on fused lithium tetraborate glass pellets with analytical precision greater than 5% at the SKLODG. Trace elements of whole rocks were analyzed using a PE DRC-e ICP–MS at the SKLODG. Approximately 50 mg of sample powder was dissolved in high-pressure Teflon bombs using an HF + $HNO_3$ mixture. Rh was used as an internal standard to monitor signal drift during analysis. The

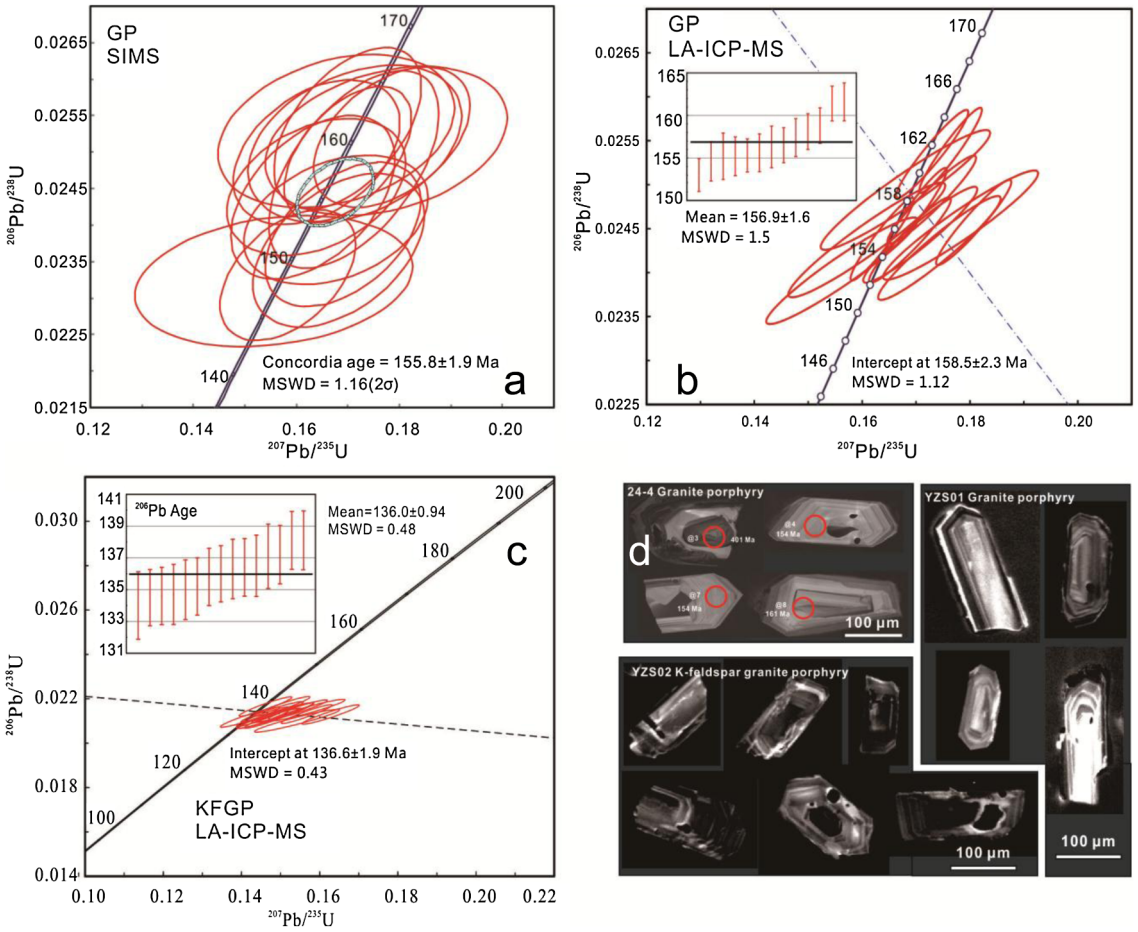


**Fig. 5.** (a) Zircon SIMS U-Pb ages of the granite porphyry (GP). (b) LA-ICP-MS U-Pb ages of the granite porphyry (GP). (c) LA-ICP-MS U-Pb ages of the K-feldspar granite porphyry (KFGP). (d) CL images of representative zircons in the LSKD.

analytical uncertainty was generally greater than 5%. The detailed analytical procedures are similar to those given in Qi et al. (2000).

Whole-rock Sr-Nd isotopic measurements were performed on a Triton thermal ionization mass spectrometer at the SKLODG and Tianjin Geological Survey Center, China Geological Survey. Samples for Sr and Nd isotopic analysis were initially dissolved in the mixture of HF, $HNO_3$, and $HClO_4$ in Teflon bombs. Sr, Rb, Sm and Nd were then separated by conventional cation exchange techniques in the HDEHP-coated Kef columns. The mass fractionation corrections for Sr and Nd isotopic ratios are based on $^{86}Sr/^{88}Sr = 0.1194$ and $^{146}Nd/^{144}Nd = 0.7219$, respectively. The $^{87}Sr/^{86}Sr$ ratio of the NBS987 Sr standard was determined to be 0.710258 ± 7 (2SD). The $^{143}Nd/^{144}Nd$ ratios of the JNDI-1 Nd standard solutions were determined to be 0.512104 ± 5 (2SD).

Lead isotope compositions of sulfides were analyzed on an IsoProbe-T thermal ionization mass spectrometer (TIMS) at the Analytical Laboratory of the Beijing Research Institute of Uranium Geology. Lead was separated and purified by a conventional anion-exchange technique (AG1 × 8, 100–200 resin) with diluted HBr used as eluant. The $^{208}Pb/^{206}Pb$, $^{207}Pb/^{206}Pb$ and $^{204}Pb/^{206}Pb$ ratios of the Standard NBS981 measured in this study were 2.1681 ± 0.0008 (2SD), 0.91464 ± 0.00033 (2SD) and 0.059042 ± 0.000037 (2SD), respectively.

## 5. Results

### 5.1. Zircon U–Pb ages and trace elements

Zircon U-Pb data obtained by SIMS and LA-ICP-MS are listed in Appendix Table A1 and A2, and representative zircon CL images and analytical spots are shown in Fig. 5. Most zircons are light pink to colorless euhedral crystals, with grain sizes of 50–200 μm and length to width ratios from 1.5:1 to 3:1 (Fig. 5). Most zircon grains show typical oscillatory and sector zoning under CL imaging, indicating their magmatic origin.

SIMS analyses of sample 24-4 from GP have shown variable contents of U (68–5012 ppm) and Th (55–1737 ppm) with high Th/U ratios of 0.3–2.1 (Appendix Table A1), indicative of magmatic zircon. Spot 24-4@12 with extreme high contents of U was excluded from the calculation based on the reliability of the age result. Spot 24-4@03 with an old $^{206}Pb/^{238}U$ age of 401 Ma was also excluded. The remaining 15 spot analyses with lower $f_{206}$ and U contents have $^{206}Pb/^{238}U$ ages ranging from 148.1 to 161.2 Ma (Fig. 5), giving a Concordia age of 155.8 ± 1.9 Ma (2SD). It is interpreted as the magma crystallization age of the granite porphyry.

Sample YZS01 was selected from Yinzhushan GP for LA-ICP-MS zircon U-Pb dating (Appendix Table A2). Thirteen analyses on 13 grains have U contents varying from 113 to 1440 ppm, and Th from 126 to 784 ppm. Th/U ratios of these zircons range between 0.5 and 1.4, with an average of 0.8. Thirteen analyses show an intercept age of 158.5 ± 2.3 Ma (Fig. 5), consistent with the weighted mean $^{206}Pb/^{238}U$ age of 156.9 ± 1.6 Ma.

Sample YZS02 from Yinzhushan KFGP was dating by LA-ICP-MS (Appendix Table A2). Fifteen analyses on 15 grains have U contents of 284–898 ppm and Th content of 328–849 ppm, with Th/U ratios between 0.6 and 1.7 (average = 1.0). All data from the 15 analyses yielded an intercept age of 136.6 ± 1.9 Ma (MSWD = 0.43; Fig. 5), consistent with the weighted mean $^{206}Pb/^{238}U$ age of 136.0 ± 0.9 Ma

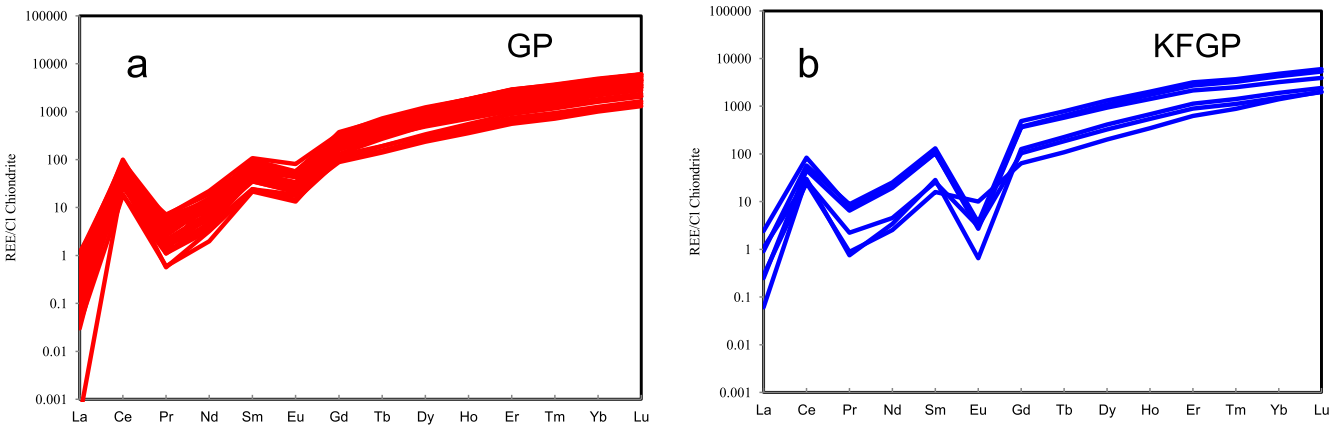


**Fig. 6.** Chondrite-normalized REE diagrams for zircons from (a) granite porphyry (GP) and (b) K-feldspar granite porphyry (KFGP) in the LSKD.

(MSWD = 0.48) within uncertainty.

A total of thirty trace element analyses of zircons were conducted for the GP and the KFGP (Appendix Table A3). Trace elements such as Hf, U, Th and REE contents were determined in situ for individual zircon grain. To avoid influence from other mineral inclusions in zircons such as apatite and titanite, during LA-ICP-MS analyses (e.g., Lu et al., 2016), we excluded the spots with Ca > 200 ppm, La > 0.3 ppm or Ti > 20 ppm that, reflect apatite and titanite contamination, respectively (Appendix Table A3). Most of the analyzed zircons show REE patterns that steeply increase from La to Lu, with pronounced positive Ce anomalies (11.03–60.95, mean = 35.48) and negative Eu anomalies (0.77–4.69, mean = 2.23) (Fig. 10 and Appendix Table A3).

The remaining analyses show low LREE and elevated HREE contents, with negative Eu and strongly positive Ce anomalies (Fig. 6). In general, zircon crystals from the GP and KFGP show distinct Eu anomalies ($Eu_N/Eu_N^* = Eu_N/(Sm_N \times Gd_N)^{0.5}$ and Ti-in-zircon temperatures (Appendix Table A3). Zircon crystals from the GP have relatively low calculated temperatures (average of 764 °C; 661–996 °C) with relatively large and uniform $Eu_N/Eu_N^*$ values from 0.24 to 0.46 (mean = 0.34). In contrast, zircon crystals from the KFGP have relatively high calculated temperatures (average of 790 °C; 664–943 °C) with relatively low $Eu_N/Eu_N^*$ values from 0.01 to 0.32 (mean = 0.07).

### 5.2. Whole rock geochemistry

Major element oxide and trace element concentrations of all samples were reported in Table 1. On the Zr/Ti versus Nb/Y diagram (Fig. 7a), the GP data straddle on the boundary between rhyolite, pantellerite, trachyandesite, and trachyte, whereas the KFGP were mainly plot within the field of pantellerite.

The KFGP shows a small range of $SiO_2$ (75.26–76.92%), $K_2O$ (5.84–6.32%), $Na_2O$ (1.14–2.31%), $Al_2O_3$ (12.39–13.61%) and $Fe_2O_3$ (0.44–1.99%). The GP shows a relatively wide range of $SiO_2$ (73.24-82.63%) with $K_2O$ (4.78–5.20%), $Na_2O$ (0.14–3.08%), $Al_2O_3$ (9.01–14.06%) and $Fe_2O_3$ (0.69–1.47%). The A/CNK ratios of all samples range from 1.2 to 3.0 with a mean of 1.5, and fall within the peraluminous field in the A/NK vs. A/CNK diagram (Fig. 7b).

All samples are enriched in light rare earth elements (LREE) (Fig. 8), with $(La/Yb)_N$ of 7.0–19.1 for the GP, and 1.8–34.3 for KFGP (Table 1). The GP exhibits relatively consistent REE features and moderate negative Eu anomalies with $Eu_N/Eu_N^*$ of 0.07–0.67, and the KFGP shows scattered REE features and strong negative Eu anomalies with $Eu_N/Eu_N^*$ of 0.02–0.05. The REE pattern of KFGP revealed in this study is consistent with the former studied one (Fig. 8).

All rocks in the LSKD are enriched in large ion lithophile elements (LILE, i.e., Rb, Th, U, K and Pb) and depleted in high field strength elements (HFSE, e.g., Nb, Ta and Ti) as well as Ba, Sr, and P (Fig. 9). The GP in this study exhibits the same trace element pattern as that of the ore-bearing granites, exception for relatively weak depletion in Ba, Sr and P, and enrichment in Pb in ore-bearing GP. The studied KFGP shows similar trace elements patterns to that of the former studied one.

### 5.3. Sr-Nd-Pb isotopes

For the samples with low Sr contents and extremely high and variable $^{87}Rb/^{86}Sr$ ratios, their calculated initial $^{87}Sr/^{86}Sr$ ratios are not meaningful to constrain their petrogenesis (e.g. Su et al., 2014; Wu et al., 2002). Hence, we only presented Nd isotopic data of granites in the LSKD in Table 2 and calculated the $\varepsilon_{Nd}(t)$ values against the respective zircon U-Pb ages in this study. The GP has $\varepsilon_{Nd}(t)$ values ranging from −10.0 to −9.7 with $T_{DM2}$ values of 1688–1915 Ma, whereas the KFGP has higher $\varepsilon_{Nd}(t)$ values ranging from −7.5 to −7.6 with younger $T_{DM2}$ values of 1538–1548 Ma.

The Lengshuikeng porphyries show similar high radiogenic Pb isotopic compositions with present-day whole-rock Pb isotopic ratios of $^{206}Pb/^{204}Pb$ = 17.853–18.365, $^{207}Pb/^{204}Pb$ = 15.571–15.606 and $^{208}Pb/^{204}Pb$ = 38.358–39.124 (Table 3). Initial Pb isotopic ratios of samples were calculated using the whole-rock Pb isotopic ratios and U, Th and Pb contents against individual zircon U-Pb ages. The calculated initial Pb isotopic ratios are $(^{206}Pb/^{204}Pb)_i$ = 17.647–17.952, $(^{207}Pb/^{204}Pb)_i$ = 15.555–15.604 and $(^{208}Pb/^{204}Pb)_i$ = 37.851–38.541. In Fig. 10, all samples lie well above the northern hemisphere reference line (NHRL) of Hart (1984), and define a positively-correlated linear array roughly parallel to the NHRL.

## 6. Discussion

### 6.1. Ages of GP and KFGP

Our dating reveal two episodes of magmatisms occurred in the LSKD, with the earlier episode around 156 Ma and the later episode from 134 Ma to 139 Ma. The granite porphyry and crystal tuff from the first member of the E'huling Formation were dated at ca. 155.6–162 Ma by LA-ICP-MS and SHRIMP zircon U-Pb dating (Zuo et al. 2010; Meng et al. 2012; Qiu et al. 2013; Su et al., 2013, 2014). Increasing studies

**Table 1**
The analytical results of major (wt.%) and trace elements (ppm) of GP and KFGP in LSKD.

| Sample | 188–1-01 | 188–1-02 | 188–1-03 | 188–1-04 | 188–1-05 | 188–1-06 | 188–1-07 | 188–1-08 | 188–1-09 | 188–1-10 | 188–1-11 | 188–1-12 | 188–1-13 |
|---|---|---|---|---|---|---|---|---|---|---|---|---|---|
| Rock type | Granite porphyry (GP) | | | | | | | | | | | | |
| $SiO_2$ | 74.85 | 77.7 | 78.09 | 78.76 | 79.78 | 77.74 | 77.13 | 75.82 | 75.39 | 75.49 | 76.65 | 76.38 | 78.39 |
| $TiO_2$ | 0.07 | 0.07 | 0.07 | 0.07 | 0.08 | 0.09 | 0.09 | 0.1 | 0.11 | 0.13 | 0.16 | 0.07 | 0.08 |
| $Al_2O_3$ | 12.54 | 12.67 | 11.77 | 12.1 | 11.02 | 12.63 | 12.69 | 13.37 | 13.6 | 12.73 | 12.38 | 12.33 | 11.83 |
| $Fe_2O_3$ | 1.86 | 1.05 | 1.48 | 1.19 | 0.87 | 1.08 | 1.02 | 1.1 | 1.2 | 1.87 | 1.54 | 2.98 | 1.43 |
| MnO | 0.8 | 0.06 | 0.15 | 0.13 | 0.03 | 0.04 | 0.04 | 0.03 | 0.02 | 0.02 | 0.03 | 0.06 | 0.04 |
| MgO | 0.19 | 0.28 | 0.33 | 0.26 | 0.25 | 0.25 | 0.33 | 0.31 | 0.28 | 0.27 | 0.37 | 0.21 | 0.28 |
| CaO | 0.14 | 0.07 | 0.58 | 0.13 | 0.02 | 0.08 | 0.02 | 0.01 | 0.02 | 0.04 | 0.01 | 0.01 | 0 |
| $Na_2O$ | 1.90 | 0.15 | 0.11 | 0.09 | 0.12 | 1.31 | 0.12 | 0.11 | 0.14 | 0.19 | 0.15 | 0.06 | 0.08 |
| $K_2O$ | 5.03 | 5.49 | 4.85 | 4.88 | 5.19 | 5.2 | 6.19 | 6.27 | 6.72 | 6.62 | 6.21 | 3.62 | 4.62 |
| $P_2O_5$ | 0.02 | 0.02 | 0.03 | 0.11 | 0.02 | 0.02 | 0.02 | 0.01 | 0.01 | 0.03 | 0.02 | 0.02 | 0.01 |
| BaO | 0.05 | 0.05 | 0.05 | 0.05 | 0.06 | 0.06 | 0.06 | 0.07 | 0.08 | 0.08 | 0.07 | 0.01 | 0.03 |
| LOI | 2.29 | 2.13 | 2.3 | 2.25 | 1.58 | 1.73 | 1.81 | 2.04 | 2.16 | 2.42 | 2.16 | 3.28 | 2.23 |
| Total | 99.7 | 99.7 | 99.8 | 100.0 | 99.0 | 100.2 | 99.5 | 99.2 | 99.7 | 99.8 | 99.7 | 99.0 | 99.0 |
| $CaO/Al_2O_3$ | 0.0 | 0.0 | 0.0 | 0.0 | 0.0 | 0.0 | 0.0 | 0.0 | 0.0 | 0.0 | 0.0 | 0.0 | 0.0 |
| $K_2O/Na_2O$ | 2.6 | 36.6 | 44.1 | 54.2 | 43.3 | 4.0 | 51.6 | 57.0 | 48.0 | 34.8 | 41.4 | 60.3 | 57.8 |
| A/NK | 1.5 | 2.0 | 2.2 | 2.2 | 1.9 | 1.6 | 1.8 | 1.9 | 1.8 | 1.7 | 1.8 | 3.1 | 2.3 |
| A/CNK | 1.4 | 2.0 | 1.8 | 2.1 | 1.9 | 1.6 | 1.8 | 1.9 | 1.8 | 1.7 | 1.8 | 3.1 | 2.3 |
| Ba | 412 | 434 | 367 | 423 | 543 | 493 | 557 | 598 | 722 | 687 | 586 | 84.7 | 231 |
| Rb | 186 | 208 | 204 | 195.5 | 187 | 183 | 240 | 265 | 259 | 270 | 268 | 178 | 207 |
| Sr | 82.5 | 57.1 | 58.6 | 70.5 | 59.4 | 83.6 | 80.6 | 76.2 | 80.2 | 83.8 | 75.4 | 46.4 | 54.5 |
| Y | 14.7 | 14.1 | 13.5 | 13.7 | 12.1 | 13.2 | 18.2 | 19.3 | 20.2 | 18.8 | 14.2 | 20.5 | 20.2 |
| Zr | 81.2 | 67 | 71 | 75.7 | 72.8 | 79.6 | 90.5 | 91 | 88.7 | 82.6 | 96.4 | 73.5 | 87.3 |
| Nb | 18.2 | 16.5 | 15.8 | 15.5 | 13.8 | 15.6 | 17.3 | 22.1 | 21.5 | 21.4 | 20.8 | 20.4 | 20.9 |
| Th | 18.2 | 15.5 | 17.6 | 16.5 | 15.4 | 15.8 | 16.9 | 16.4 | 10.7 | 20 | 12.1 | 17.8 | 18.6 |
| Pb | 37 | 19.5 | 26.7 | 192.5 | 58.9 | 36.4 | 177 | 66.3 | 78.1 | 139 | 30.2 | 1430 | 241 |
| Ga | 16.2 | 15.2 | 15.3 | 14.15 | 12.2 | 14.6 | 15.5 | 16.8 | 16.6 | 16.6 | 18 | 17.6 | 15.4 |
| Zn | 13.5 | 14.3 | 14.8 | 505.1 | 82.1 | 16.7 | 146.2 | 236.6 | 317.2 | 93.9 | 83.3 | 992.5 | 93.9 |
| Cu | 9.4 | 13.0 | 5.4 | 16.8 | 12.8 | 3.6 | 16.4 | 4.5 | 3.4 | 18.1 | 4.6 | 9.6 | 3.5 |
| Ni | 1.59 | 1.54 | | 0.93 | 2.19 | 1.80 | 1.21 | 0.79 | 0.32 | 0.60 | 0.34 | 0.01 | |
| V | 6.03 | 4.98 | 6.71 | 6.24 | 6.95 | 7.07 | 6.8 | 6.61 | 6.51 | 11.9 | 14.8 | 3.19 | 3.29 |
| Cr | 20.8 | 13.9 | 14.1 | 13.8 | 16.7 | 19.5 | 14.1 | 7.21 | 8.54 | 10.5 | 9.65 | 8.45 | 14.5 |
| Hf | 2.99 | 2.28 | 2.64 | 2.655 | 2.26 | 2.62 | 2.88 | 3.04 | 3.27 | 3.07 | 3.38 | 2.74 | 3.06 |
| Cs | 4.14 | 5.01 | 3.28 | 4.71 | 3.63 | 3.36 | 3.18 | 8.77 | 7.22 | 7.34 | 6.32 | 3.47 | 3.30 |
| Sc | 3.80 | 2.70 | 2.59 | 2.30 | 1.94 | 2.87 | 2.90 | 3.48 | 3.14 | 3.90 | 4.17 | 2.43 | 2.98 |
| Ta | 1.53 | 1.41 | 1.46 | 1.26 | 1.13 | 1.22 | 1.30 | 1.69 | 1.84 | 1.67 | 1.68 | 1.75 | 1.72 |
| Co | 0.81 | 0.58 | 0.80 | 0.79 | 0.88 | 1.02 | 0.52 | 0.67 | 1.11 | 1.37 | 1.11 | 0.31 | 0.61 |
| Ag | 0.35 | 0.81 | 1.01 | 1.87 | 0.53 | 1.51 | 2.03 | 2.33 | 0.25 | 1.23 | 0.54 | 1.95 | 1.72 |
| U | 5.33 | 4.42 | 4.26 | 5.64 | 4.27 | 4.69 | 4.58 | 4.99 | 4.60 | 5.62 | 4.36 | 5.61 | 6.07 |
| La | 27.30 | 27.00 | 26.60 | 26.70 | 24.80 | 26.40 | 28.10 | 31.50 | 30.50 | 32.00 | 36.00 | 26.10 | 22.90 |
| Ce | 54.80 | 53.90 | 53.50 | 53.40 | 49.70 | 53.00 | 56.30 | 63.60 | 61.80 | 64.50 | 70.70 | 55.60 | 48.80 |
| Pr | 5.89 | 5.78 | 5.73 | 5.62 | 5.33 | 5.60 | 5.95 | 6.95 | 6.64 | 6.79 | 7.57 | 6.10 | 5.31 |
| Nd | 20.60 | 19.80 | 19.90 | 19.60 | 18.40 | 19.30 | 20.00 | 23.70 | 23.40 | 23.60 | 25.60 | 21.80 | 18.90 |
| Sm | 4.01 | 3.46 | 3.91 | 3.58 | 3.44 | 3.57 | 3.81 | 4.47 | 4.44 | 4.73 | 4.47 | 4.74 | 4.15 |
| Eu | 0.56 | 0.59 | 0.63 | 0.69 | 0.56 | 0.48 | 0.57 | 0.52 | 0.55 | 0.54 | 0.56 | 0.70 | 0.45 |
| Gd | 3.07 | 2.34 | 2.74 | 2.81 | 2.45 | 2.79 | 3.08 | 3.60 | 3.53 | 3.55 | 3.06 | 3.47 | 3.23 |
| Tb | 0.52 | 0.48 | 0.53 | 0.50 | 0.40 | 0.44 | 0.57 | 0.60 | 0.59 | 0.61 | 0.49 | 0.64 | 0.58 |
| Dy | 2.73 | 2.43 | 2.65 | 2.355 | 2.12 | 2.38 | 3.01 | 3.12 | 3.14 | 3.2 | 2.32 | 3.29 | 3.23 |
| Ho | 0.54 | 0.49 | 0.47 | 0.48 | 0.39 | 0.44 | 0.59 | 0.64 | 0.58 | 0.64 | 0.45 | 0.61 | 0.64 |
| Er | 1.45 | 1.38 | 1.39 | 1.315 | 1.17 | 1.21 | 1.52 | 1.7 | 1.83 | 1.78 | 1.37 | 1.82 | 1.67 |
| Tm | 0.21 | 0.20 | 0.21 | 0.21 | 0.16 | 0.17 | 0.22 | 0.26 | 0.28 | 0.27 | 0.22 | 0.27 | 0.27 |
| Yb | 1.38 | 1.15 | 1.21 | 1.225 | 1.19 | 1.32 | 1.5 | 1.62 | 1.73 | 1.76 | 1.35 | 1.72 | 1.63 |
| Lu | 0.20 | 0.19 | 0.19 | 0.17 | 0.17 | 0.18 | 0.22 | 0.24 | 0.26 | 0.22 | 0.22 | 0.27 | 0.22 |

**Table 1** *(continued)*

| Sample | 188–1-01 | 188–1-02 | 188–1-03 | 188–1-04 | 188–1-05 | 188–1-06 | 188–1-07 | 188–1-08 | 188–1-09 | 188–1-10 | 188–1-11 | 188–1-12 | 188–1-13 |
|---|---|---|---|---|---|---|---|---|---|---|---|---|---|
| Rock type | Granite porphyry (GP) | | | | | | | | | | | | |
| ΣREE | 123 | 119 | 120 | 119 | 110 | 117 | 125 | 143 | 139 | 144 | 154 | 127 | 112 |
| $Eu_N/Eu_N^*$ | 0.49 | 0.64 | 0.59 | 0.67 | 0.59 | 0.47 | 0.51 | 0.40 | 0.42 | 0.41 | 0.46 | 0.52 | 0.37 |
| Sr/Y | 5.6 | 4.0 | 4.3 | 5.1 | 4.9 | 6.3 | 4.4 | 3.9 | 4.0 | 4.5 | 5.3 | 2.3 | 2.7 |
| Rb/Sr | 2.3 | 3.6 | 3.5 | 2.8 | 3.1 | 2.2 | 3.0 | 3.5 | 3.2 | 3.2 | 3.6 | 3.8 | 3.8 |
| $(La/Yb)_N$ | 16.8 | 15.8 | 15.6 | 14.9 | 14.3 | 13.4 | 13.9 | 12.6 | 13.0 | 19.1 | 10.9 | 10.1 | 7.0 |
| Sample | 188–1-14 | 188–1-15 | 188–1-16 | | L24-3 | L24-4 | L24-5 | L24-6 | 188–2-01 | 188–2-02 | 188–2-03 | 188–2-04 | 188–2-05 |
| Rock type | Granite porphyry (GP) | | | | | | | | K-feldspar granite porphyry (KFGP) | | | | |
| $SiO_2$ | 73.33 | 75.22 | 73.62 | | 73.24 | 73.9 | 79.9 | 82.6 | 75.67 | 75.99 | 76.92 | 75.26 | 76.47 |
| $TiO_2$ | 0.07 | 0.07 | 0.06 | | 0.21 | 0.24 | 0.12 | 0.1 | 0.09 | 0.09 | 0.09 | 0.09 | 0.08 |
| $Al_2O_3$ | 12.34 | 12.43 | 11.26 | | 14.06 | 13.9 | 11.5 | 9.01 | 12.84 | 13.61 | 12.39 | 12.4 | 12.7 |
| $Fe_2O_3$ | 2.46 | 1.55 | 2.43 | | 1.36 | 1.47 | 0.69 | 1.26 | 1.19 | 0.85 | 1.39 | 1.99 | 0.99 |
| MnO | 1.74 | 1.12 | 2.15 | | 0.05 | 0.02 | | 0.01 | 0.01 | 0.01 | 0.01 | 0.01 | 0.01 |
| MgO | 0.26 | 0.27 | 0.33 | | 0.33 | 0.41 | 0.29 | 0.21 | 0.06 | 0.06 | 0.06 | 0.04 | 0.05 |
| CaO | 0.07 | 0.05 | 0.16 | | 0.13 | 0.14 | | 0.01 | 0.01 | 0.01 | | | 0.01 |
| $Na_2O$ | 0.15 | 0.16 | 0.13 | | 3.08 | 3.00 | 0.60 | 0.14 | 2.31 | 1.14 | 1.87 | 1.89 | 2.09 |
| $K_2O$ | 6.6 | 6.75 | 5.78 | | 5.2 | 5.1 | 4.84 | 4.78 | 5.84 | 6.32 | 5.95 | 6.05 | 6.1 |
| $P_2O_5$ | 0.01 | 0.02 | 0.05 | | 0.05 | 0.07 | 0.03 | 0.03 | 0.01 | 0.01 | 0.01 | 0.01 | 0.01 |
| BaO | 0.05 | 0.05 | 0.04 | | 0.05 | 0.06 | 0.1 | 0.08 | 0.02 | 0.02 | 0.04 | 0.02 | 0.03 |
| LOI | 3.23 | 2.45 | 3.5 | | 1.58 | 1.7 | 2 | 1.65 | 1.2 | 1.95 | 1.24 | 1.42 | 1.06 |
| Total | 100.3 | 100.1 | 99.5 | | 99.4 | 100.0 | 100.1 | 99.9 | 99.2 | 100.0 | 99.9 | 99.2 | 99.6 |
| $CaO/Al_2O_3$ | 0.0 | 0.0 | 0.0 | | 0.0 | 0.0 | 0.0 | 0.0 | 0.0 | 0.0 | 0.0 | 0.0 | 0.0 |
| $K_2O/Na_2O$ | 44.0 | 42.2 | 44.5 | | 1.7 | 1.7 | 8.1 | 34.1 | 2.5 | 5.5 | 3.2 | 3.2 | 2.9 |
| A/NK | 1.7 | 1.6 | 1.7 | | 1.3 | 1.3 | 1.8 | 1.7 | 1.3 | 1.6 | 1.3 | 1.3 | 1.3 |
| A/CNK | 1.6 | 1.6 | 1.7 | | 1.3 | 1.3 | 1.8 | 1.7 | 1.3 | 1.6 | 1.3 | 1.3 | 1.3 |
| Ba | 467.5 | 440 | 422 | | 582 | 699 | 969 | 841 | 145 | 96.1 | 267 | 105 | 154 |
| Rb | 273 | 274 | 244 | | 186 | 177 | 180 | 173 | 302 | 290 | 249 | 270 | 199 |
| Sr | 70 | 75 | 74.4 | | 102 | 99.2 | 15.6 | 18.2 | 65.9 | 54.7 | 60 | 52.1 | 52.3 |
| Y | 21.2 | 21.9 | 21.6 | | 24.4 | 26.5 | 16.6 | 32.3 | 43.6 | 32.3 | 35.1 | 42.3 | 36.6 |
| Zr | 89.35 | 72.9 | 72.8 | | 131 | 106 | 75.5 | 91.2 | 249 | 245 | 216 | 226 | 217 |
| Nb | 22.3 | 21.4 | 19.9 | | 29.0 | 28.4 | 25.1 | 22.1 | 36.8 | 32.8 | 31.0 | 33.9 | 32.0 |
| Th | 21.7 | 19.3 | 19.7 | | 25.9 | 25.4 | 22.3 | 20.1 | 41.9 | 30 | 24.1 | 31.8 | 29.6 |
| Pb | 38.9 | 229 | 212 | | 26.9 | 18.4 | 14.4 | 56.3 | 43.6 | 21.3 | 77.8 | 42.2 | 19.5 |
| Ga | 17.15 | 16.8 | 17 | | 17.7 | 18.1 | 14 | 11.3 | 17.6 | 15.2 | 14.8 | 16.7 | 14.6 |
| Zn | 445.7 | 534.3 | 816.1 | | 100.5 | 91.6 | 9.2 | 24.8 | 123.2 | 177.2 | 118.7 | 145.3 | 77.8 |
| Cu | 11.7 | 9.8 | 5.5 | | 1.9 | 2.5 | 2.4 | 5.0 | 9.0 | 5.6 | 6.5 | 10.0 | 2.9 |
| Ni | 2.04 | | 0.82 | | 0.88 | 1.01 | 0.99 | 4.31 | 4.44 | | 0.86 | 0.74 | |
| V | 2.715 | 2.59 | 2.95 | | 19.1 | 19.6 | 10 | 6.26 | 2.39 | 1.38 | 1.27 | 0.865 | 0.672 |
| Cr | 12.25 | 9.01 | 9.95 | | 1.14 | 2.22 | 1.72 | 4.38 | 14 | 4.25 | 8.5 | 4.88 | 5.12 |
| Hf | 3.545 | 2.87 | 2.72 | | 3.84 | 3.47 | 2.58 | 3.75 | 8.29 | 7.66 | 6.99 | 7.82 | 7.21 |
| Cs | 7.25 | 5.45 | 4.10 | | 4.29 | 4.45 | 3.13 | 2.79 | 4.07 | 3.49 | 3.35 | 3.37 | 3.54 |
| Sc | 3.87 | 3.40 | 2.73 | | 4.78 | 5.47 | 2.64 | 1.84 | 5.95 | 3.83 | 4.51 | 4.71 | 2.75 |
| Ta | 1.95 | 1.95 | 1.73 | | 2.30 | 2.28 | 2.42 | 1.60 | 2.15 | 2.00 | 1.81 | 2.08 | 1.93 |
| Co | 0.71 | 0.54 | 0.64 | | 92.00 | 94.40 | 78.70 | 80.10 | 0.28 | 0.15 | 0.18 | 0.13 | 0.12 |
| Ag | 6.08 | 3.03 | 3.92 | | 0.54 | 1.08 | 0.53 | 0.33 | 0.42 | 0.36 | 0.53 | 0.30 | 0.25 |
| U | 7.59 | 7.30 | 9.46 | | 3.77 | 5.37 | 5.66 | 3.80 | 6.26 | 5.55 | 4.99 | 5.77 | 5.62 |
| La | 19.40 | 22.50 | 21.20 | | 37.30 | 42.60 | 28.20 | 12.00 | 28.30 | 32.80 | 9.68 | 13.60 | 57.80 |
| Ce | 41.95 | 47.90 | 44.20 | | 80.10 | 55.60 | 52.80 | 28.90 | 51.40 | 73.20 | 22.10 | 50.10 | 70.00 |
| Pr | 4.60 | 5.29 | 4.88 | | 8.22 | 9.16 | 6.25 | 3.57 | 5.96 | 8.03 | 2.24 | 3.16 | 11.40 |
| Nd | 16.70 | 19.00 | 17.70 | | 27.80 | 31.20 | 21.50 | 14.60 | 20.70 | 27.40 | 8.17 | 11.10 | 38.30 |
| Sm | 4.06 | 4.42 | 3.93 | | 5.15 | 5.97 | 4.68 | 4.46 | 4.24 | 5.94 | 1.88 | 2.72 | 6.84 |

**Table 1** *(continued)*

| Sample | 188–1-14 | 188–1-15 | 188–1-16 | L24-3 | L24-4 | L24-5 | L24-6 | 188–2-01 | 188–2-02 | 188–2-03 | 188–2-04 | 188–2-05 |
|---|---|---|---|---|---|---|---|---|---|---|---|---|
| Rock type | Granite porphyry (GP) | | | | | | | K-feldspar granite porphyry (KFGP) | | | | |
| Eu | 0.36 | 0.49 | 0.59 | 0.52 | 0.67 | 0.32 | 0.10 | 0.05 | 0.05 | 0.01 | 0.04 | 0.05 |
| Gd | 3.57 | 3.40 | 3.87 | 4.19 | 4.72 | 3.63 | 4.54 | 4.41 | 4.72 | 2.49 | 3.46 | 5.69 |
| Tb | 0.64 | 0.65 | 0.63 | 0.75 | 0.83 | 0.61 | 0.89 | 1.01 | 0.96 | 0.73 | 1.01 | 1.12 |
| Dy | 3.7 | 3.8 | 3.49 | 4.21 | 4.61 | 2.94 | 5.4 | 6.99 | 5.69 | 5.7 | 6.78 | 6.35 |
| Ho | 0.73 | 0.70 | 0.68 | 0.85 | 0.93 | 0.62 | 1.19 | 1.62 | 1.18 | 1.32 | 1.52 | 1.37 |
| Er | 2.06 | 2.08 | 1.91 | 2.49 | 2.55 | 1.8 | 3.35 | 4.73 | 3.31 | 3.87 | 4.52 | 3.9 |
| Tm | 0.29 | 0.30 | 0.30 | 0.35 | 0.40 | 0.29 | 0.50 | 0.73 | 0.51 | 0.58 | 0.68 | 0.52 |
| Yb | 1.99 | 1.92 | 1.95 | 2.19 | 2.37 | 1.72 | 3.17 | 4.35 | 3.11 | 3.77 | 4.36 | 3.51 |
| Lu | 0.30 | 0.28 | 0.27 | 0.32 | 0.36 | 0.24 | 0.47 | 0.69 | 0.43 | 0.53 | 0.69 | 0.52 |
| ΣREE | 100 | 113 | 106 | 174 | 162 | 126 | 83 | 135 | 167 | 63 | 104 | 207 |
| $Eu_N/Eu_N^*$ | 0.29 | 0.39 | 0.46 | 0.34 | 0.38 | 0.24 | 0.07 | 0.04 | 0.03 | 0.02 | 0.04 | 0.03 |
| Sr/Y | 3.3 | 3.4 | 3.4 | 4.2 | 3.7 | 0.9 | 0.6 | 1.5 | 1.7 | 1.7 | 1.2 | 1.4 |
| Rb/Sr | 3.9 | 3.7 | 3.3 | 1.8 | 1.8 | 11.5 | 9.5 | 4.6 | 5.3 | 4.2 | 5.2 | 3.8 |
| $(La/Yb)_N$ | 8.4 | 7.8 | 12.2 | 12.9 | 11.8 | 2.7 | 36.9 | 4.7 | 7.6 | 1.8 | 2.2 | 11.8 |

LOI = loss on ignition. $(La/Yb)_N$ normalised data after Sun and McDonald (1989).

have shown extensive magmatic and mineralization activities in the Late Jurassic also occurred in the NWA. Zircons of granites from the Yongping Cu deposit, Zhoujia Pb-Zn deposit, and Xiongjiashan Mo deposit yielded U-Pb ages within 155–164.6 Ma using LA-ICP-MS (Ding et al, 2005; Qin, 2011; Qiu et al., 2015). The molybdenites Re-Os ages range from 155.7 to 162.8 Ma for the Yongping Cu deposit and the Xiongjiashan Mo deposit (Li et al., 2007; Meng et al., 2007).

The late Jurassic magmatism occurred not only in the NWA, but also in a wide range of Nanling as an important W-Sn metallogenic province in China. Mao et al. (2007) proposed that the large-scale W-Sn mineralization and associated magmatism in Nanling occurred during the Middle to Late Jurassic (i.e., 165–150 Ma). The metallogenic ages (e.g. Molybdenite Re-Os and cassiterite U-Pb, Yao et al., 2005, 2007; Yuan et al., 2008, 2011, 2018), zircons U-Pb ages and muscovite Ar-Ar ages of ore-related granites (Ma et al., 2006; Guo et al., 2011; Yuan et al., 2018, 2019; Zhang et al., 2011) are highly consistent. Therefore, the early magmatism (155.8 Ma) in the LSKD are consistent with the North Wuyi and Nanling geological events between 165 and 150 Ma (Mao et al. 2007), implying widespread mineralization and magmatism across South China during this period.

The late episode magmatism (134–139 Ma) is similar to the volcanic-intrusive rock ages of ~144–137 Ma (except for granite porphyry) in Tianhuashan Basin (Su et al., 2013). A wide range of mineralization and magmatism in Early Cretaceous also occurred in the NWA. The host rhyodacite and rhyodacitic porphyry rocks from the Xiangshan uranium deposit in the western NWA, yielded LA-ICP-MS zircon $^{206}Pb/^{238}U$ ages of 135.1 ± 1.7 and 134.8 ± 1.1 Ma, respectively (Yang et al., 2012). The Shengmikeng vein-type Pb-Zn ore deposit situated in the Huanggangshan Basin 30 km to the east of the LSKD (see Fig. 1), gave a SHRIMP zircon U-Pb age of 138.3 ± 1.4 Ma for the host potassic trachyte porphyry (Luo et al., 2009). Zhang et al. (2009) obtained a molybdenite Re-Os age (135.5 ± 5.7 Ma) in the recently discovered Jinzhuping polymetallic deposit which is genetically associated with the concealed granite pluton in the Lizikeng basin, 80 km to the northeast of the LSKD (Fig. 1). The early magmatism and mineralization mainly distributed in Nanling, while the late magmatism (139–134 Ma) in the NWA show more similar distribution to magmatism in the lower Yangtze (Zhou et al., 2012), North Jiangxi Province (Feng et al., 2012; Huang and Jiang, 2014), Northwest Zhejiang Province and South Anhui Province (Wu et al., 2012; Xie et al., 2012), and the coastal area (JH, Li et al., 2014). These show a wide range of magmatism and mineralization in South China. Meanwhile, evidence from mafic rocks in the GHTB and A-type granites in its adjacent regions indicates the extension peak may have occurred from 130 to 120 Ma (ZL, Li et al., 2013b; Qi et al., 2012, 2016).

### 6.2. Petrogenesis

#### 6.2.1. Alteration effects

Petrographic observations show various degrees of alteration in the studied samples represented by differences in total major elements contents and LOI values (1.06–3.50%). During alteration, Ca, Na, K, and LILE (e.g., Rb, Sr, and Ba) are generally mobile (e.g., Zhou 1999). In Harker diagrams ($SiO_2$ versus selected major elements; Fig. 7), the alkali elements ($K_2O$ and $Na_2O$) are significantly scattered. This is most likely due to hydrothermal alteration as indicated by a rough correlation between the alkali contents ($K_2O$ + $Na_2O$) and LOI.

#### 6.2.2. Genetic type

The S-type granites are characterized by peraluminous (ACNK > 1.1), high Rb low Sr contents, and presence of aluminous primary minerals, such as muscovite, cordierite, tourmaline, andalusite, and garnet (Chappell and White, 2001). The two studied granites in the LSKD are both strongly peraluminous, with high alkali oxides contents ($K_2O$ + $Na_2O$ = 3.7–6.9% for GP; 7.5–8.3%, for the KFGP) and rich in K ($K_2O/Na_2O$ = 2.65–60.33, mean = 41.65, for the GP; 2.53–5.54,

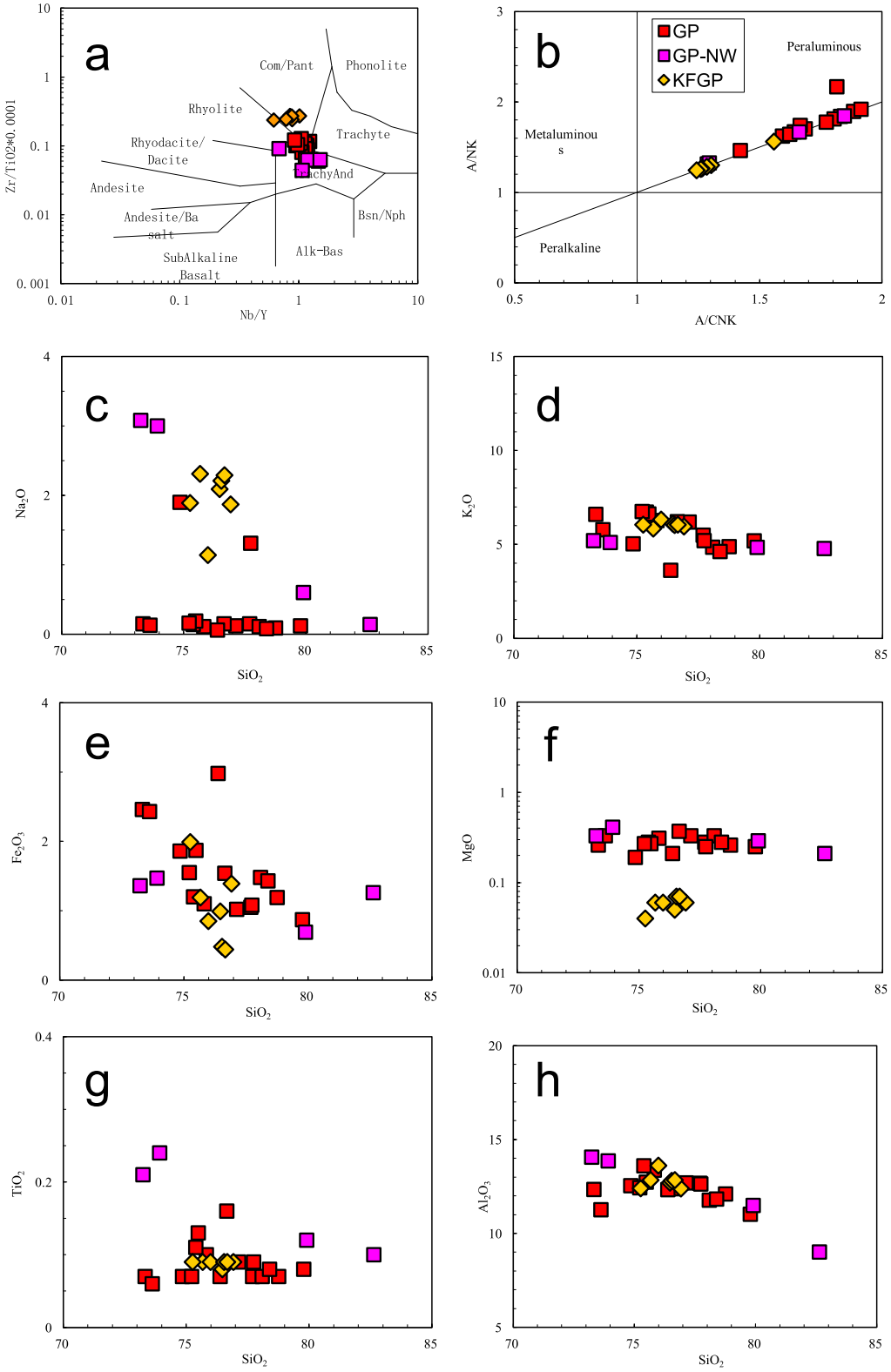


**Fig. 7.** (a) Zr/Ti vs. Nb/Y (Winchester and Floyd, 1977); (b) A/NK vs. A/CNK; (c) $Na_2O$ vs. $SiO_2$; (d) $K_2O$ vs. $SiO_2$; (e) $Fe_2O_3$ vs. $SiO_2$; (f) MgO vs. $SiO_2$; (g) $TiO_2$ vs. $SiO_2$; and (h) $Al_2O_3$ vs. $SiO_2$ Harker diagram for the granite porphyry (GP), and the K-feldspar granite porphyry (KFGP) in the LSKD.

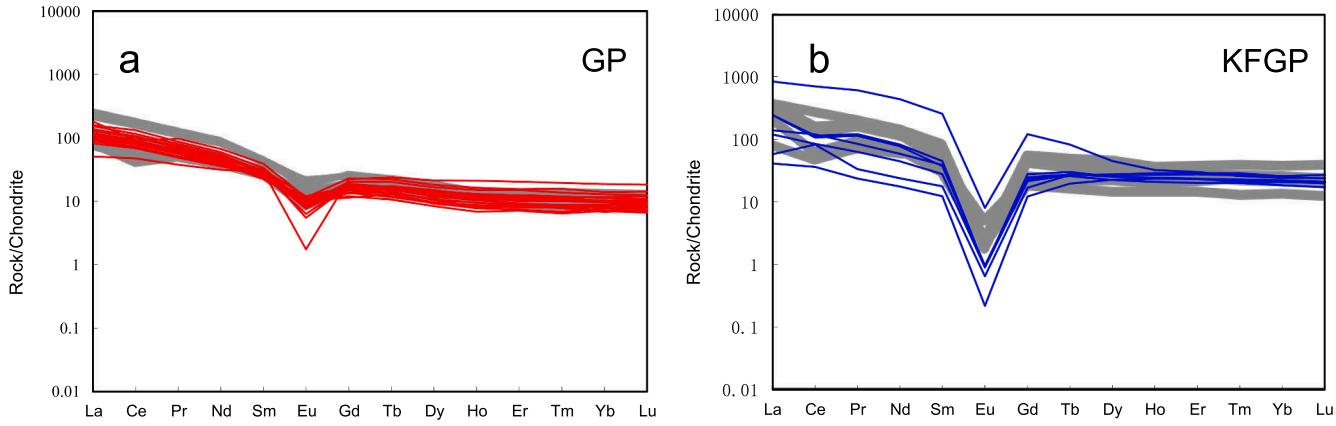


**Fig. 8.** Chondrite-normalized REE diagrams for (a) granite porphyry (GP) and (b) K-feldspar granite porphyry (KFGP) in LSKD. REE abundances for chondrite are after Sun and McDonough (1989). Grey areas are data of granite porphyry and K-feldspar granite porphyry from Su et al. (2014), and CM, Wang et al. (2013).

mean = 3.25 for the KFGP). They also have high $Al_2O_3$ contents (11.02–13.60%, mean = 12.36% for the GP; 12.39–13.61%, Mean = 12.80% for the KFGP) and contain primary muscovite. The typical I-type granites indicators of hornblende (Chappell and White, 2001) and relatively low Rb/Sr ratios (< 0.9) (e.g. Wang et al., 1993) are not consistent with the studied samples which have no hornblende present with relative high Rb/Sr ratios of 2.2–3.9 for the GP and 3.8–16.1, for the KFGP. Therefore, we suggest the studied granites in the LSKD are likely S-type granites.

### 6.2.3. Petrogenesis

Despite some elements are mobile during alteration, the alteration processes do not significantly affect HFSE and REE even during the most intensive hydrothermal alteration (Pearce et al., 1992). Both the relatively fresh samples and the highly altered granite samples in the LSKD show subparallel REE patterns (except for Eu) and HFSE concentrations, indicating these rocks still preserve their original REE and HFSE signatures. In addition, the relatively constant $\varepsilon_{Nd}(t)$ values in studied samples indicate negligible effects of alteration on Nd-isotope composition. $Fe_2O_3$, MgO, $TiO_2$, and $Al_2O_3$ show roughly correlated trends with $SiO_2$ (Fig. 7), suggesting they may not be in a broadly cogenetic suite. Similar evidence is from the different trace element compositions, REE and Eu anomalies ($Eu_N/Eu_N^*$) of two granites. However, the identical $\varepsilon_{Nd}(t)$ and previous zircon Hf isotopes suggest that these rocks possibly originated from similar source materials.

As for the GP, the obvious negative $\varepsilon_{Nd}(t)$ values of −10.0 to −9.7 suggest that they were most probably derived from ancient crustal rocks. The zircon $\varepsilon_{Hf}(t)$ values of felsic rocks from the Tianhuashan basin with the highest values concentrated between −6 and −10 (Su et al., 2014) also support their crustal rock sources. In addition, previous studies have shown the Cathaysia Block has a Paleo- to Mesoproterozoic basement, which consists mainly of schists, granulites, and amphibolites (e.g., Fletcher et al., 2004; Jiang et al., 2006; Ling et al., 1998; Su and Zhang, 2012). As for the KFGP, the relative higher $\varepsilon_{Nd}(t)$ values of −7.6 to −7.5 compared to the GP, suggests that minor mantle contribution involved in its petrogenesis, despite that they share similar magma source to the GP. Based on their relatively low whole-rock CaO, $Fe_2O_3$, MgO contents, the low-grade meta-sedimentary rock rich of muscovite and biotite may be the most likely candidate source rock. This is also supported by the Pb isotopic compositions (Table 3, Fig. 10). In summary, these features suggest that the GP and KFGP may have different melting conditions such as temperatures, source materials and contents of aqueous fluids, etc.

Pervasive free aqueous fluids do not exist in the continental crust at depths greater than the uppermost few kilometers (Yardley and Valley, 1997), except where low-grade rocks are rapidly underthrusted beneath higher-grade rocks (Patiño Douce, 1999). Dehydration melting of hydrous minerals, such as muscovite, biotite, and amphibolite, in the

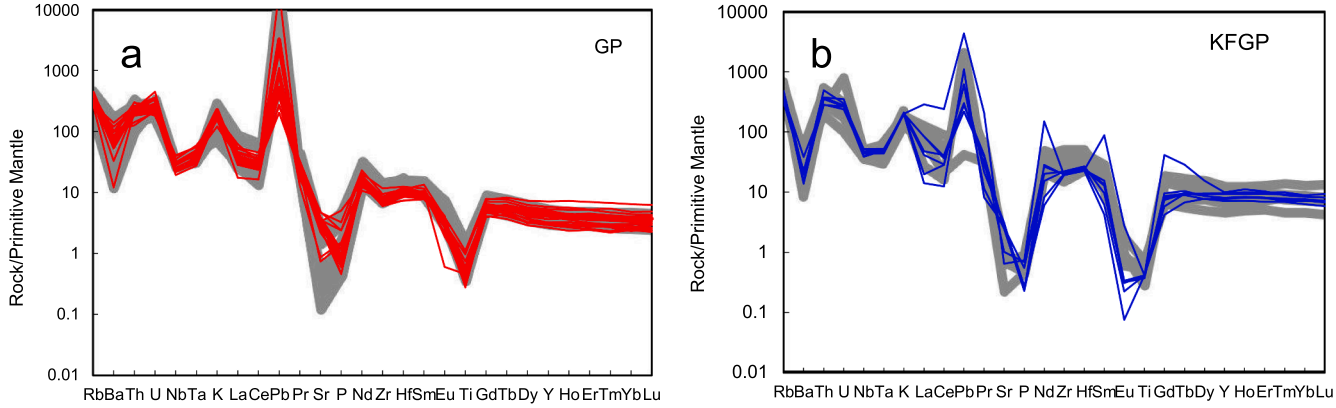


**Fig. 9.** Primitive mantle-nor malized trace element diagram for (a) the granite porphyry (GP) and (b) the K-feldspar granite porphyry (KFGP) in the LSKD. The primitive mantle values are after Sun and McDonough (1989). Grey areas are data of granite porphyry and K-feldspar granite porphyry from Su et al. (2014) and Wang et al. (2013).

**Table 2**
Whole-rock Nd isotope compositions for granites in LSKD.

| Sample | Rock Type | Age | $^{147}Sm/^{144}Nd$ | $^{143}Nd/^{144}Nd$ | ± 2σ | $^{143}Nd/^{144}Nd_i$ | $\varepsilon Nd_t$ | $T_{DM}$(Ma) | $T_{DM2}$(Ma) |
|---|---|---|---|---|---|---|---|---|---|
| 24-3 | GP | 156 | 0.1080 | 0.512048 | 0.000002 | 0.511938 | −9.7 | 1586 | 1735 |
| 24-4 | GP | 156 | 0.1175 | 0.512058 | 0.000003 | 0.511938 | −9.7 | 1726 | 1734 |
| 24-5 | GP | 156 | 0.1311 | 0.512060 | 0.000002 | 0.511926 | −10.0 | 2005 | 1752 |
| 24-6 | GP | 156 | 0.1914 | 0.512126 | 0.000004 | 0.511931 | −9.9 | 6850 | 1714 |
| 24-28 | KFGP | 137 | 0.1148 | 0.512173 | 0.000002 | 0.512071 | −7.6 | 1502 | 1548 |
| 24-29 | KFGP | 137 | 0.1070 | 0.512173 | 0.000008 | 0.512078 | −7.5 | 1392 | 1538 |

Note: all the initial isotopic ratios were corrected to the corresponding zircon ages. Sm and Nd abundances for the samples were determined by ICP-MS. $\varepsilon_{Nd}(t)$ values are calculated using present-day $(^{147}Sm/^{144}Nd)_{CHUR}$ = 0.1967 and $(^{143}Nd/^{144}Nd)_{CHUR}$ = 0.512638. $T_{DM}$ values are calculated using present-day $(^{147}Sm/^{144}Nd)_{DM}$ = 0.2137 and $(^{143}Nd/^{144}Nd)_{DM}$ = 0.51315.The details for single-($T_{DM1}$) or two-stage ($T_{DM2}$) Nd model age calculations are given by Wu et al. (2002). Two-stage Nd model age ($T_{DM2}$) is calculated using the same formulation as Keto and Jacobsen (1987).

continental crust is an important mechanism of magma formation (Patiño Douce, 1999). The Cs and U are exclusively concentrated in magmas formed from direct melting of meta-sedimentary rock sources, and are not elevated in magmas that have experienced an earlier episode of melting (Dostal and Capedri, 1978; Förster et al., 1999). For the GP and KFGP, the weak correlation between U, Cs and $SiO_2$ (Fig. 11) indicates the high U and Cs concentrations may not have resulted from the evolution of the magma but inherited from the magma source (Hall et al., 1993). The GP has a relative higher Cs concentration than the KFGP, and relative low Ti-in-Zircon temperatures, suggesting GP may be from direct melting of these fertile meta-sedimentary rock sources and experienced an earlier episode of melting (Dostal and Capedri, 1978; Förster et al., 1999). The accordant U value may be from the main rock-forming minerals such as biotite and muscovite, rather than from amphiboles that are rich in U than Cs (Dostal and Capedri, 1978). The KFGP has a younger $T_{DM2}$ values with a relative high $\varepsilon_{Nd}(t)$ (−7.6 to −7.5) compared to the GP ($\varepsilon_{Nd}(t)$, −10.0 to −9.7), indicating minor contribution from mantle-derived magmas occurred in younger granite.

Based on the above discussion, we suggest both studied rocks from the LSKD were mainly formed from the dehydration melting of fertile Proterozoic meta-sedimentary rocks. The early GP experienced relatively low temperature melting with more contribution of aqueous fluids from dehydration, whereas the later KFGP with higher melting temperature may obtain more materials and heat from the mantle. Mafic rocks in GHTB and A-type granites in the adjacent regions of NWA indicate that the extension peak occurred from 130 to 120 Ma (Li et al., 2013b; Qi et al, 2016). The mantle contribution could have probably played an important role in an extensional geodynamic setting in the later period (Qi et al., 2012, 2016).

The rare presence of zircons with old ages in the studied samples, except for one age of 401 Ma in the GP, and a few other spots in the KFPG, and lack of wall rock-derived enclaves indicate very limited effects of wall-rock contamination. Hence, we propose rare crustal contamination occurred in the genesis of studied rocks in the LSKD. We favor the interpretation that felsic volcanic-intrusions could undergo fractional crystallization in the upper crustal level (Li et al., 2013b). Fractionation of plagioclase can result in negative Sr and Eu anomalies, whereas fractionation of K-feldspar leads to negative Ba and Eu anomalies. In addition, the high Rb/Sr ratios of granites also indicate

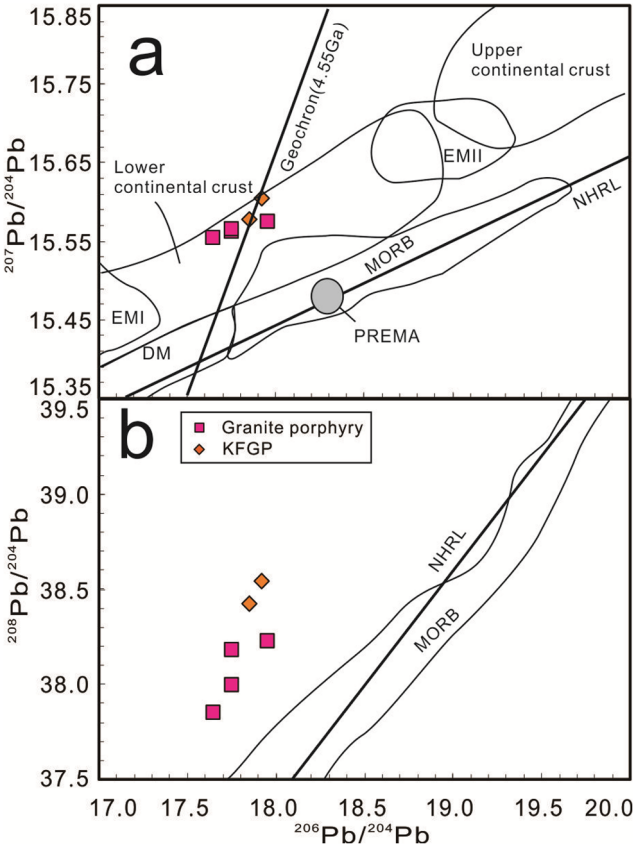


**Fig. 10.** Pb isotopic ratios for the granite porphyry (GP), and the K-feldspar granite porphyry (KFGP) in the LSKD. (a) $^{207}Pb/^{204}Pb$ vs. $^{206}Pb/^{204}Pb$; (b) $^{208}Pb/^{204}Pb$ vs. $^{206}Pb/^{204}Pb$. Fields for depleted mantle (DM), prevalent mantle (PREMA), enrichment mantle I and II (EMI and EMII), and upper and lower continental crust are after Zindler and Hart (1986); Pacific mid-ocean ridge basalt (MORB) are after Zou et al. (2000); and the NHRL (Northern Hemisphere Reference Line) is after Hart (1984).

**Table 3**
Whole-rock Pb isotopic data of granites from LSKD.

| Sample | Rock Type | Age | $^{206}Pb/^{204}Pb$ | 2 σ | $^{207}Pb/^{204}Pb$ | 2 σ | $^{208}Pb/^{204}Pb$ | 2 σ | $(^{206}Pb/^{204}Pb)_i$ | $(^{207}Pb/^{204}Pb)_i$ | $(^{208}Pb/^{204}Pb)_i$ |
|---|---|---|---|---|---|---|---|---|---|---|---|
| 24-3 | GP | 159 | 18.170 | 0.002 | 15.586 | 0.002 | 38.718 | 0.004 | 17.952 | 15.575 | 38.229 |
| 24-4 | GP | 159 | 18.099 | 0.001 | 15.577 | 0.001 | 38.550 | 0.003 | 17.647 | 15.555 | 37.851 |
| 24-5 | GP | 159 | 18.365 | 0.001 | 15.592 | 0.001 | 38.784 | 0.003 | 17.751 | 15.562 | 37.994 |
| 24-6 | GP | 159 | 17.853 | 0.002 | 15.571 | 0.001 | 38.358 | 0.003 | 17.749 | 15.566 | 38.178 |
| 24-28 | KFGP | 136.5 | 17.954 | 0.001 | 15.606 | 0.001 | 38.587 | 0.003 | 17.922 | 15.604 | 38.541 |
| 24-29 | KFGP | 136.5 | 18.342 | 0.003 | 15.602 | 0.002 | 39.124 | 0.006 | 17.852 | 15.578 | 38.425 |

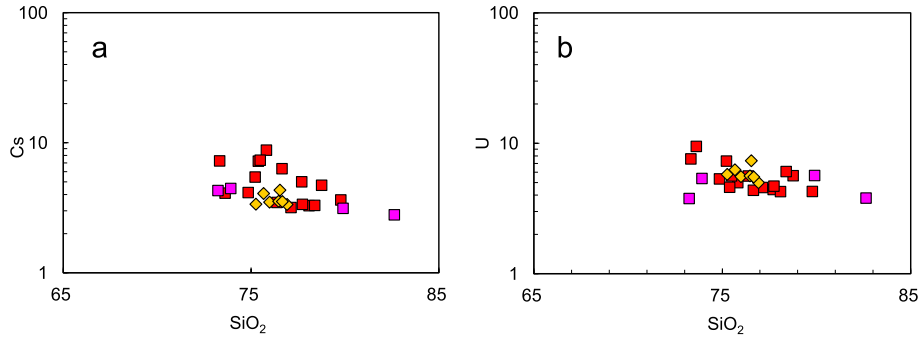


**Fig. 11.** (a) Cs vs. $SiO_2$; and (b) U vs. $SiO_2$ diagrams.

high degrees of fractionation of plagioclase (Bouseilly and EI Sokkary, 1975). Moreover, the studied granites show enrichment of LILE (e.g., Rb, Th, and K) and depletion of Ba, Nb, Sr, Eu and Ti (Fig. 9), implying fractional crystallization of feldspar and ilmenite/magnetite.

In summary, both granites were dominantly derived from the dehydration melting of fertile Proterozoic meta-sedimentary rocks, with more contribution of dehydration fluids to the GP and relatively more mantle contribution to the KFGP. Both granites underwent fractional crystallization of plagioclase, K-feldspar and ilmenite/magnetite followed by minor assimilation of the upper crust.

### 6.3. Relatively oxidized hydrous magma

Previous studies have shown magmatic oxidation state ($fO_2$), water, sulfur and chlorine contents in associated magma could play important roles in the formation of porphyry Cu deposits (e.g., Burnham, 1979; Candela, 1992; Richards, 2003; Loucks, 2014). The magma with a high oxygen fugacity ($fO_2$) may have been more conducive to the mineralization of chalcophile elements (Cu, Au, Mo, Ag etc. e.g. Richards, 2003). Because the behavior of chalcophile elements is controlled by sulfide, and the speciation and behavior of sulfur are controlled by oxygen fugacity. Hence, it is speculated that a relatively high oxygen fugacity may also be a necessary condition for the formation of a porphyry silver deposit. In addition, high water content can facilitate the melting of magma source and much more formation of hydrothermal fluids, contributing to the metallogenesis at a late stage (Richards, 2011; Wang et al., 2014b,c). However, it is difficult to estimate the original magmatic water contents from variable altered granites. The geochemistry characteristics of associated and barren granites can help us to roughly assess the water content of magma source.

The ore-forming magmas often show distinctive whole-rock chemical signatures, such as high Sr/Y and Eu/Eu* ratios, which can be used as ore fertility indicators of high magmatic water and sulfur contents (Richards and Kerrich, 2007; Chiaradia et al., 2012; Loucks, 2014), and high oxidation states of magma (Streck and Dilles, 1998; Chambefort et al., 2008; Richards, 2011; Wang et al., 2014b,c; Lu et al., 2015). In this study, the GP and KFGP in the LSKD show relatively low Sr/Y ratios and high Y contents, different from the high Sr/Y ratios and low Y features of associated granites in the porphyry Cu ± Mo ± Au deposits. These features indicate amphibole may not be a major mineral in their magma source, and the water content of magma associated with porphyry Ag deposits is lower than that of magma related to porphyry Cu deposits, and should be in a relatively moderate level. Furthermore, early plagioclase crystallization can be suppressed due to the presence of water in hydrous magmas (Moore and Carmichael, 1998), resulting in no pronounced depletion of Eu in melts ($Eu^{2+}$ substitutes for $Ca^{2+}$ in plagioclase). Therefore, the whole-rock moderate negative Eu anomalies for GP could further suggest more water content in the GP magma than that in the KFGP as indicated by its strong negative Eu anomalies.

However, whole-rock Sr/Y and Eu/Eu* ratios are easily affected by

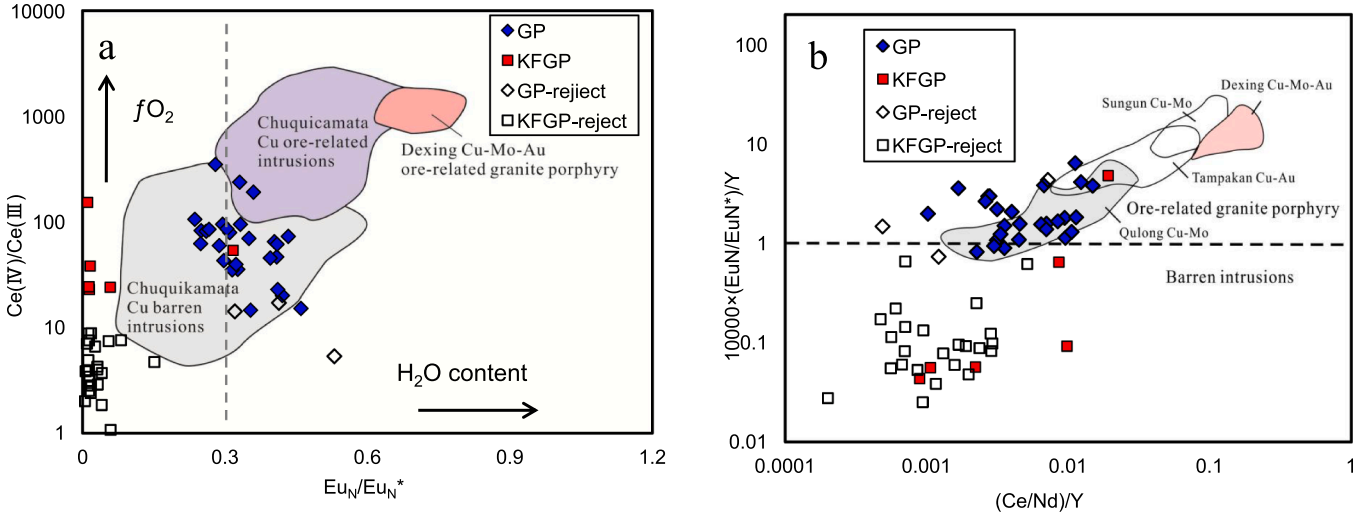


**Fig. 12.** (a) Zircon Ce(IV)/Ce(III) vs. $Eu_N$ /$Eu_N$*; and (b) 10000 × ($Eu_N$/$Eu_N$*)/Y vs. (Ce/Nd)/Y diagrams. Dexing data in (a) are after Zhang et al., (2013) and Chuquicamata data are after Ballard et al., (2002). All data in (b) are after Lu et al., (2016).

weathering or hydrothermal alteration. As a ubiquitous mineral in intermediate to felsic igneous rocks, zircon could survive intense hydrothermal alteration and weathering and record the compositional evolution and varying conditions of the parent melts (Ballard et al., 2002; Claiborne et al., 2010; Kemp et al., 2011; Dilles et al., 2015). Many studies have shown that trace element compositions in zircon are sensitive to magmatic water content (Wang et al., 2014b; Lu et al., 2016; Zhu et al., 2018) and oxygen fugacity (Ballard et al., 2002; Liang et al., 2006; Wang et al., 2014c; Dilles et al., 2015; Lu et al., 2016; Xu et al., 2016; Loader et al., 2017; Zhu et al., 2018).

Zircon $Ce^{4+}/Ce^{3+}$ ratio could be regarded as an indicator of magmatic oxidation state (Ballard et al., 2002). However, because La and Pr abundances are low and close to the analytical detection limit, Dilles et al. (2015) and Lu et al. (2016) argued it was difficult to accurately estimate oxygen fugacity values when using La and Pr as a baseline to calculate the Ce anomaly. Considering that, we calculated and compared the zircon $Ce^{4+}/Ce^{3+}$ ratios of the GP and KFGP to assess the relative oxygen fugacity of magma using the method of Ballard et al. (2002), after excluding the data with contents of Ca > 200 ppm, La > 0.3 ppm or Ti > 20 ppm. For comparison, we also calculated the element ratios (e.g. Ce(IV)/Ce(III) and (Ce/Nd)/Y) of spots that had been rejected due to high contents of Ca, La and Ti. The GP generally has much higher zircon Ce(IV)/Ce(III) ratios than the post-mineralization KFGP, suggesting the GP has a relatively high $fO_2$ than the barren KFGP (Fig. 12). The lower Ce(IV)/Ce(III) ratios in the rejected spots compared to selected spots in the KFGP, suggest great influence from high-La minerals. However, limited data of the KFGP hinder further discussion on the oxygen fugacity of magma. Lu et al. (2016) found that Ce(IV)/Ce(III) and Ce/Nd have an exponential relationship and they suggested the Ce/Nd ratio in zircon can be an alternative method to estimate the amplitude of the Ce anomaly. In Fig. 12, the roughly consistent ranges of (Ce/Nd)/Y between selected and rejected data indicate that using zircon (Ce/Nd)/Y can effectively reduce the interference of high La content. The GP generally has much higher zircon (Ce/Nd)/Y (average = 0.006) values than the KFGP (average = 0.003), indicating more oxidized conditions in GP magma. We speculate that the high oxygen fugacity in the GP may be inherited from the crust, and this is consistent with much more negative $\varepsilon_{Nd}(t)$ values ($-10.0 \sim -9.7$) in the GP than the $\varepsilon_{Nd}(t)$ values ($-7.6 \sim -7.5$) in the KFGP.

$Eu^{3+}$ as the predominant valence state in oxidized magmas, can be easily partitioned into zircon along with other REE (Ballard et al., 2002; Hoskin and Schaltegger, 2003; Trail et al., 2011, 2012; Dilles et al., 2015). Considering the suppression of plagioclase crystallization in water-rich magmas and its strong incorporation of Eu, relatively elevated negative Eu anomalies in zircons could indicate relatively high magmatic water contents and/or oxidation states (Ballard et al., 2002; Dilles et al., 2015; Lu et al., 2016). Lu et al. (2016) proposed fertile magmatic suites have collectively higher zircon Eu/Eu* (> 0.3) and 10,000 × (Eu/Eu*)/Y (> 1) than infertile suites in porphyry Cu system.

In the zircon $Eu_N/Eu_N^*$ vs. Ce(IV)/Ce(III) diagram (Fig. 12), the GP data plot in the field between the associated granites and barren granites in the porphyry Cu deposit, indicating a relatively moderate oxygen fugacity for the porphyry Ag deposit. In addition, the zircon 10,000 × $(Eu_N/Eu_N^*)$/Y values range from 0.82 to 6.40 with a mean of 2.14 for the GP and from 0.04 to 4.79 with a mean of 0.95 for the KFGP. The higher 10,000 × $(Eu_N/Eu_N^*)$/Y values of the GP are attributed to the suppression of plagioclase crystallization under more water system (Lu et al., 2016), consistent with the high water melting conditions in the GP. On the other hand, using the Ti-in-zircon thermometer, the causative GP has much lower temperatures (average of 764 ℃; range = 661–996 ℃) than the barren KFGP (average of 790 ℃; range = 664–943 ℃). As mentioned above, both granites result from partial melting of ancient crusts, and the addition of water in the formation of granites can effectively lower the melting temperature. The lower melting temperature of the GP indicates more water content in its magma source compared to the KFGP.

In conclusion, our comparison of magmatic oxidized hydrous conditions shows that magma associated with porphyry silver deposit probably has a relatively moderate oxidation state and water content.

## 7. Conclusions

Whole rock major and trace elements, Nd-Pb isotopes, and Zircon U-Pb ages and trace element analyses of the Mesozoic associated GP and barren KFGP in the LSKD, NWA have allowed us to reach the following conclusions:

(1) The GP related to Ag mineralization was emplaced in 156 Ma, and the barren KFGP was emplaced in 137 Ma. Both granites are peraluminous and akin to typical S-type granites;
(2) The GP and KFGP were predominantly derived from dehydration melting of Proterozoic *meta*-sedimentary rocks, with more dehydration fluids contribution to the GP and relatively more mantle contribution to the KFGP. Both granites underwent fractional crystallization of plagioclase, K-feldspar and ilmenite/magnetite followed by minor assimilation of upper-crust;
(3) The comparison of magmatic oxidizing hydrous conditions shows that relatively moderate oxidation state and water content in associated magma are probably important factors in porphyry silver mineralization.

## CRediT authorship contribution statement

**Youqiang Qi:** Conceptualization, Funding acquisition, Methodology, Project administration, Investigation, Visualization, Writing - original draft, Writing - review & editing. **Ruizhong Hu:** Conceptualization. **Jianfeng Gao:** Conceptualization, Funding acquisition, Methodology, Project administration, Writing - original draft, Writing - review & editing. **Chengbiao Leng:** Investigation. **Haotian Gong:** Visualization. **Wei Gao:** Investigation.

## Declaration of Competing Interest

The authors declare that they have no known competing financial interests or personal relationships that could have appeared to influence the work reported in this paper.

## Acknowledgments

This research is financially supported by the National Key Research and Development Program of China (No. 2016YFC0600207), the National Natural Science Foundation of China (Grant No. 41973049, 40903018) to Dr. Qi, and the National Key Basic Research Program (Grant No. 2012CB416705). We thank Prof. X.H. Li, Dr. D.F. He and Dr. Z.B. Xiao for their help in analyses and technical assistance. We are grateful to Prof. C.S. Li for his help in improving the manuscript.

## Appendix A

See Appendix Tables A1–A3.

**Appendix Table A1**
SIMS zircon U–Pb isotopic analysis of mineralized granite porphyry from LSKD, South China.

| Dating spot No. | U ppm | Th ppm | Th/U | $f_{206}$ % | $^{207}Pb/^{206}Pb$ | ± 1σ % | $^{207}Pb/^{235}U$ | ± 1σ % | $^{206}Pb/^{238}U$ | ± 1σ % | $t_{207/235}$ Ma | ± 1σ | $t_{206/238}$ Ma | ± 1σ |
|---|---|---|---|---|---|---|---|---|---|---|---|---|---|---|
| *Graniteporphyry 24-4* | | | | | | | | | | | | | | |
| 24-4@01 | 236 | 218 | 0.9 | 0.00 | 0.04857 | 3.51 | 0.1633 | 3.98 | 0.0244 | 1.87 | 154 | 6 | 155 | 3 |
| 24-4@02 | 203 | 346 | 1.7 | 0.14 | 0.05034 | 2.51 | 0.1584 | 3.38 | 0.0233 | 1.57 | 149 | 5 | 149 | 2 |
| 24-4@03 | 204 | 55 | 0.3 | 0.09 | 0.05546 | 1.50 | 0.4851 | 2.29 | 0.0642 | 1.55 | 402 | 8 | 401 | 6 |
| 24-4@04 | 79 | 102 | 1.3 | 0.17 | 0.04849 | 4.03 | 0.1639 | 4.32 | 0.0245 | 1.56 | 154 | 6 | 156 | 2 |
| 24-4@05 | 125 | 142 | 1.1 | 0.00 | 0.05138 | 3.22 | 0.1691 | 3.64 | 0.0239 | 1.69 | 159 | 5 | 152 | 3 |
| 24-4@06 | 80 | 124 | 1.6 | 0.34 | 0.04951 | 4.62 | 0.1714 | 4.94 | 0.0251 | 1.75 | 161 | 7 | 160 | 3 |
| 24-4@07 | 94 | 106 | 1.1 | 0.28 | 0.04759 | 3.68 | 0.1640 | 4.02 | 0.0250 | 1.62 | 154 | 6 | 159 | 3 |
| 24-4@08 | 122 | 215 | 1.8 | 0.00 | 0.05015 | 3.25 | 0.1712 | 3.94 | 0.0248 | 2.23 | 160 | 6 | 158 | 3 |
| 24-4@09 | 86 | 76 | 0.9 | 0.00 | 0.05056 | 4.09 | 0.1678 | 4.35 | 0.0241 | 1.50 | 158 | 6 | 153 | 2 |
| 24-4@10 | 125 | 106 | 0.8 | 0.00 | 0.05139 | 3.10 | 0.1786 | 3.47 | 0.0252 | 1.55 | 167 | 5 | 160 | 2 |
| 24-4@11 | 68 | 72 | 1.1 | 0.00 | 0.04813 | 5.33 | 0.1678 | 5.59 | 0.0253 | 1.69 | 158 | 8 | 161 | 3 |
| 24-4@13 | 87 | 170 | 1.9 | 0.59 | 0.05323 | 3.74 | 0.1557 | 7.07 | 0.0232 | 1.57 | 147 | 10 | 148 | 2 |
| 24-4@14 | 147 | 183 | 1.2 | 0.18 | 0.04869 | 2.94 | 0.1700 | 3.43 | 0.0253 | 1.78 | 159 | 5 | 161 | 3 |
| 24-4@15 | 76 | 160 | 2.1 | 0.00 | 0.05119 | 5.14 | 0.1775 | 5.40 | 0.0252 | 1.65 | 166 | 8 | 160 | 3 |
| 24-4@16 | 138 | 212 | 1.5 | 0.00 | 0.05159 | 3.60 | 0.1683 | 4.03 | 0.0237 | 1.81 | 158 | 6 | 151 | 3 |
| 24-4@17 | 335 | 415 | 1.2 | 0.14 | 0.05050 | 2.14 | 0.1701 | 2.96 | 0.0250 | 1.51 | 159 | 4 | 159 | 2 |

**Appendix Table A2**
LA–ICP–MS U–Pb isotopic data for zircons for GP and KFGP from LSKD, South China.

| | | | | Isotopic ratios | | | | | | Age (Ma) | | | | | |
|---|---|---|---|---|---|---|---|---|---|---|---|---|---|---|---|
| Spot | Th | U | Th/U | $^{207}Pb/^{206}Pb$ | 1σ | $^{207}Pb/^{235}U$ | 1σ | $^{206}Pb/^{238}U$ | 1σ | $^{207}Pb/^{235}U$ | 1σ | $^{206}Pb/^{238}U$ | 1σ | $^{208}Pb/^{232}Th$ | 1σ |
| *Granite porphyry* | | | | | | | | | | | | | | | |
| YZS01-02 | 161 | 113 | 1.42 | 0.0472 | 0.0028 | 0.1563 | 0.0093 | 0.0240 | 0.0004 | 147 | 3 | 153 | 2 | 171 | 3 |
| YZS01-06 | 753 | 1171 | 0.64 | 0.0534 | 0.0014 | 0.1807 | 0.0046 | 0.0246 | 0.0003 | 169 | 4 | 157 | 2 | 135 | 3 |
| YZS01-09 | 762 | 1440 | 0.53 | 0.0504 | 0.0011 | 0.1764 | 0.0038 | 0.0254 | 0.0003 | 165 | 6 | 162 | 2 | 145 | 4 |
| YZS01-12 | 784 | 1172 | 0.67 | 0.0499 | 0.0011 | 0.1701 | 0.0037 | 0.0247 | 0.0003 | 160 | 6 | 157 | 2 | 137 | 5 |
| YZS01-13 | 542 | 754 | 0.72 | 0.0495 | 0.0013 | 0.1730 | 0.0044 | 0.0254 | 0.0003 | 162 | 5 | 161 | 2 | 141 | 5 |
| YZS01-15 | 279 | 193 | 1.45 | 0.0527 | 0.0029 | 0.1783 | 0.0095 | 0.0245 | 0.0004 | 167 | 7 | 156 | 2 | 161 | 5 |
| YZS01-16 | 295 | 313 | 0.94 | 0.0507 | 0.0021 | 0.1708 | 0.0070 | 0.0244 | 0.0004 | 160 | 5 | 156 | 2 | 156 | 4 |
| YZS01-18 | 532 | 713 | 0.75 | 0.0503 | 0.0015 | 0.1689 | 0.0050 | 0.0244 | 0.0003 | 159 | 8 | 155 | 3 | 150 | 5 |
| YZS01-19 | 639 | 1112 | 0.57 | 0.0521 | 0.0023 | 0.1744 | 0.0075 | 0.0243 | 0.0004 | 163 | 7 | 155 | 2 | 123 | 4 |
| YZS01-21 | 140 | 256 | 0.54 | 0.0479 | 0.0029 | 0.1609 | 0.0096 | 0.0244 | 0.0004 | 152 | 6 | 155 | 2 | 118 | 6 |
| YZS01-23 | 126 | 174 | 0.72 | 0.0489 | 0.0031 | 0.1681 | 0.0104 | 0.0249 | 0.0005 | 158 | 5 | 159 | 2 | 143 | 7 |
| YZS01-28 | 344 | 493 | 0.70 | 0.0505 | 0.0016 | 0.1729 | 0.0054 | 0.0248 | 0.0003 | 162 | 5 | 158 | 2 | 153 | 4 |
| YZS01-29 | 560 | 834 | 0.67 | 0.0487 | 0.0011 | 0.1637 | 0.0039 | 0.0244 | 0.0003 | 154 | 3 | 155 | 2 | 134 | 3 |
| *K-feldspar granite porphyry* | | | | | | | | | | | | | | | |
| YZS02-01 | 480 | 503 | 0.95 | 0.0489 | 0.0015 | 0.1462 | 0.0045 | 0.0217 | 0.0003 | 139 | 4 | 138 | 2 | 119 | 3 |
| YZS02-02 | 356 | 498 | 0.71 | 0.0521 | 0.0017 | 0.1545 | 0.0050 | 0.0215 | 0.0003 | 146 | 4 | 137 | 2 | 119 | 4 |
| YZS02-04 | 548 | 625 | 0.88 | 0.0533 | 0.0015 | 0.1567 | 0.0043 | 0.0213 | 0.0003 | 148 | 4 | 136 | 2 | 120 | 3 |
| YZS02-05 | 663 | 658 | 1.01 | 0.0501 | 0.0018 | 0.1478 | 0.0053 | 0.0214 | 0.0003 | 140 | 5 | 137 | 2 | 118 | 4 |
| YZS02-06 | 362 | 327 | 1.10 | 0.0530 | 0.0021 | 0.1570 | 0.0063 | 0.0215 | 0.0003 | 148 | 6 | 137 | 2 | 116 | 4 |
| YZS02-09 | 627 | 540 | 1.16 | 0.0497 | 0.0015 | 0.1454 | 0.0044 | 0.0212 | 0.0003 | 138 | 4 | 135 | 2 | 107 | 3 |
| YZS02-10 | 705 | 898 | 0.79 | 0.0505 | 0.0019 | 0.1470 | 0.0055 | 0.0211 | 0.0003 | 139 | 5 | 135 | 2 | 118 | 5 |
| YZS02-12 | 328 | 538 | 0.61 | 0.0487 | 0.0017 | 0.1422 | 0.0050 | 0.0212 | 0.0003 | 135 | 4 | 135 | 2 | 123 | 4 |
| YZS02-14 | 518 | 405 | 1.28 | 0.0510 | 0.0018 | 0.1505 | 0.0052 | 0.0214 | 0.0003 | 142 | 5 | 136 | 2 | 119 | 4 |
| YZS02-15 | 838 | 671 | 1.25 | 0.0501 | 0.0015 | 0.1457 | 0.0043 | 0.0211 | 0.0003 | 138 | 4 | 135 | 2 | 116 | 4 |
| YZS02-16 | 849 | 507 | 1.68 | 0.0554 | 0.0017 | 0.1628 | 0.0049 | 0.0213 | 0.0003 | 153 | 4 | 136 | 2 | 113 | 3 |
| YZS02-19 | 401 | 489 | 0.82 | 0.0503 | 0.0016 | 0.1504 | 0.0047 | 0.0217 | 0.0003 | 142 | 4 | 138 | 2 | 117 | 4 |
| YZS02-20 | 331 | 284 | 1.16 | 0.0532 | 0.0025 | 0.1542 | 0.0072 | 0.0210 | 0.0003 | 146 | 6 | 134 | 2 | 117 | 5 |
| YZS02-25 | 332 | 492 | 0.67 | 0.0507 | 0.0016 | 0.1476 | 0.0046 | 0.0211 | 0.0003 | 140 | 4 | 135 | 2 | 103 | 3 |
| YZS02-26 | 597 | 531 | 1.12 | 0.0514 | 0.0016 | 0.1516 | 0.0046 | 0.0214 | 0.0003 | 143 | 4 | 136 | 2 | 116 | 4 |

**Appendix Table A3**
LA-ICP-MS zircon trace elements for GP and KFGP from LSKD, South China[1].

| Analyzed Spot | Ca | Ti | Y | Hf | Th | U | La | Ce | Pr | Nd | Sm | Eu | Gd |
|---|---|---|---|---|---|---|---|---|---|---|---|---|---|
| *Granite porphyry* | | | | | | | | | | | | | |
| YZS01-01 | Below LOD | 10.58 | 1193 | 9118 | 299 | 269 | 0.21 | 28.7 | 0.67 | 8.87 | 12.07 | 2.72 | 45.73 |
| YZS01-02 | Below LOD | 12.00 | 1285 | 9632 | 161 | 113 | 0.06 | 15.5 | 0.48 | 7.23 | 10.55 | 3.26 | 44.51 |
| YZS01-03 | Below LOD | 4.64 | 722 | 10,758 | 123 | 191 | 0.07 | 17.0 | 0.11 | 1.92 | 3.70 | 0.84 | 19.94 |
| YZS01-04 | Below LOD | 4.71 | 631 | 9613 | 75 | 94 | 0.01 | 11.0 | 0.11 | 1.56 | 3.67 | 1.08 | 18.20 |
| YZS01-05 | 153 | 12.49 | 3043 | 11,877 | 842 | 1389 | 0.20 | 43.4 | 0.45 | 4.56 | 13.08 | 3.27 | 71.49 |
| YZS01-06 | Below LOD | 2.42 | 3051 | 12,721 | 753 | 1171 | 0.02 | 35.0 | 0.25 | 5.08 | 13.69 | 2.65 | 76.83 |
| YZS01-07 | Below LOD | 2.24 | 2648 | 11,438 | 736 | 1229 | 0.02 | 33.5 | 0.20 | 3.58 | 9.29 | 1.81 | 58.90 |
| YZS01-08 | Below LOD | 3.97 | 1966 | 13,224 | 444 | 826 | 0.08 | 40.0 | 0.15 | 2.90 | 7.24 | 1.81 | 44.01 |
| YZS01-09 | Below LOD | 3.69 | 2295 | 12,512 | 762 | 1440 | 0.16 | 44.9 | 0.15 | 2.05 | 5.85 | 1.34 | 42.32 |
| YZS01-10 | Below LOD | 7.97 | 2264 | 12,644 | 910 | 1077 | 0.13 | 61.0 | 0.31 | 4.19 | 9.57 | 2.58 | 52.95 |
| YZS01-11 | Below LOD | 15.21 | 2764 | 11,287 | 590 | 681 | 0.10 | 56.6 | 0.32 | 4.51 | 9.57 | 3.26 | 55.27 |
| YZS01-12 | Below LOD | 3.95 | 2153 | 12,609 | 784 | 1172 | 0.01 | 52.1 | 0.10 | 2.29 | 6.43 | 1.51 | 42.30 |
| YZS01-13 | Below LOD | 4.66 | 2214 | 10,948 | 542 | 754 | 0.02 | 38.2 | 0.28 | 4.88 | 9.85 | 2.52 | 54.50 |
| YZS01-14 | 92 | 12.45 | 2557 | 13,882 | 1112 | 1320 | 0.22 | 54.9 | 0.59 | 6.46 | 14.92 | 3.31 | 69.08 |
| YZS01-15 | Below LOD | 6.74 | 2124 | 9916 | 279 | 193 | 0.05 | 22.4 | 0.65 | 10.35 | 16.42 | 4.69 | 70.65 |
| YZS01-18 | Below LOD | 5.67 | 1839 | 10,128 | 532 | 713 | 0.01 | 53.5 | 0.15 | 3.09 | 6.74 | 1.74 | 38.35 |
| YZS01-19 | Below LOD | 6.98 | 3145 | 12,994 | 639 | 1112 | 0.03 | 52.5 | 0.38 | 5.59 | 13.04 | 2.92 | 70.23 |
| YZS01-20 | Below LOD | 5.70 | 2198 | 12,871 | 889 | 1352 | 0.08 | 47.7 | 0.20 | 3.10 | 7.95 | 1.95 | 48.38 |
| YZS01-21 | Below LOD | 3.51 | 949 | 12,452 | 140 | 256 | 0.00 | 21.0 | 0.05 | 1.49 | 3.47 | 1.03 | 22.05 |
| YZS01-22 | Below LOD | 7.71 | 1374 | 11,376 | 190 | 167 | 0.02 | 19.2 | 0.29 | 5.02 | 8.79 | 2.50 | 39.73 |
| YZS01-23 | Below LOD | 6.39 | 845 | 10,739 | 126 | 174 | 0.04 | 16.8 | 0.14 | 2.95 | 5.41 | 1.23 | 25.01 |
| YZS01-24 | Below LOD | 2.41 | 1498 | 13,089 | 374 | 744 | 0.04 | 11.6 | 0.06 | 0.92 | 3.32 | 0.77 | 27.05 |
| YZS01-25 | Below LOD | 4.64 | 2452 | 12,204 | 645 | 1193 | 0.04 | 32.0 | 0.17 | 2.91 | 7.60 | 1.68 | 48.86 |
| YZS01-26 | Below LOD | 4.84 | 1798 | 10,888 | 382 | 431 | 0.06 | 35.8 | 0.40 | 6.34 | 10.90 | 3.06 | 51.36 |
| YZS01-28 | Below LOD | 4.86 | 1978 | 10,415 | 344 | 493 | 0.05 | 39.8 | 0.30 | 5.05 | 10.22 | 3.16 | 54.39 |
| YZS01-29 | Below LOD | 2.79 | 1579 | 11,550 | 560 | 834 | 0.26 | 48.0 | 0.18 | 2.68 | 5.36 | 1.25 | 32.85 |
| YZS01-30 | Below LOD | 7.32 | 1556 | 10,937 | 285 | 293 | 0.27 | 25.8 | 0.12 | 6.38 | 10.21 | 2.87 | 44.62 |
| *K-feldspar granite porphyry* | | | | | | | | | | | | | |
| YZS02-05 | Below LOD | 4.69 | 2898 | 10,613 | 663 | 658 | 0.06 | 28.0 | 0.62 | 9.10 | 15.84 | 0.19 | 76.80 |
| YZS02-07 | Below LOD | 2.97 | 1174 | 10,972 | 290 | 419 | 0.01 | 18.3 | 0.07 | 1.59 | 4.33 | 0.04 | 26.07 |
| YZS02-15 | Below LOD | 5.73 | 3342 | 9217 | 838 | 671 | 0.22 | 35.0 | 0.84 | 11.74 | 20.00 | 0.21 | 100.24 |
| YZS02-16 | Below LOD | 8.01 | 2407 | 7742 | 849 | 507 | 0.57 | 51.0 | 0.73 | 9.60 | 16.23 | 0.16 | 74.90 |
| YZS02-27 | Below LOD | 6.99 | 908 | 9333 | 212 | 257 | 0.26 | 16.6 | 0.21 | 2.13 | 3.92 | 0.18 | 21.27 |
| YZS02-29 | Below LOD | 4.77 | 662 | 9488 | 276 | 547 | 0.07 | 15.1 | 0.08 | 1.19 | 2.43 | 0.59 | 13.09 |

| Analyzed Spot | Tb | Dy | Ho | Er | Tm | Yb | Lu | ΣREE | Ce(IV)/Ce(III) | $Eu_N/Eu_N^*$ | $10000 \times (Eu_N/Eu_N^*)/Y$ | (Ce/Nd)/Y | T (°C)[2] |
|---|---|---|---|---|---|---|---|---|---|---|---|---|---|
| *Granite porphyry* | | | | | | | | | | | | | |
| YZS01-01 | 11.58 | 124.7 | 40.3 | 172.8 | 32.4 | 281.4 | 53.4 | 815 | 14.60 | 0.35 | 2.966 | 0.003 | 802 |
| YZS01-02 | 12.09 | 131.8 | 43.5 | 191.8 | 35.1 | 308.2 | 59.5 | 864 | 15.16 | 0.46 | 3.580 | 0.002 | 815 |
| YZS01-03 | 5.80 | 68.7 | 23.7 | 109.0 | 21.3 | 193.1 | 37.9 | 503 | 43.04 | 0.30 | 4.120 | 0.012 | 722 |
| YZS01-04 | 5.24 | 59.9 | 20.1 | 92.1 | 18.3 | 170.7 | 33.2 | 435 | 65.09 | 0.40 | 6.398 | 0.011 | 724 |
| YZS01-05 | 27.08 | 310.6 | 102.3 | 470.0 | 89.9 | 804.0 | 152.1 | 2092 | 35.58 | 0.33 | 1.074 | 0.003 | 820 |
| YZS01-06 | 25.24 | 298.3 | 104.1 | 482.2 | 91.5 | 801.5 | 151.3 | 2088 | 82.79 | 0.25 | 0.819 | 0.002 | 667 |
| YZS01-07 | 19.68 | 241.8 | 87.2 | 414.8 | 80.4 | 715.5 | 135.4 | 1802 | 105.95 | 0.24 | 0.893 | 0.004 | 661 |
| YZS01-08 | 15.10 | 186.5 | 66.1 | 309.1 | 61.1 | 549.5 | 101.7 | 1385 | 79.37 | 0.31 | 1.577 | 0.007 | 708 |
| YZS01-09 | 15.61 | 202.7 | 76.3 | 368.3 | 73.4 | 663.5 | 127.3 | 1624 | 81.66 | 0.26 | 1.134 | 0.010 | 702 |
| YZS01-10 | 17.76 | 210.9 | 75.1 | 349.4 | 67.6 | 601.7 | 114.2 | 1567 | 69.81 | 0.35 | 1.548 | 0.006 | 773 |
| YZS01-11 | 18.86 | 238.2 | 86.5 | 415.8 | 83.6 | 763.2 | 142.8 | 1879 | 72.95 | 0.43 | 1.568 | 0.005 | 841 |
| YZS01-12 | 15.04 | 190.7 | 71.6 | 340.0 | 66.9 | 603.0 | 116.0 | 1508 | 350.02 | 0.28 | 1.300 | 0.011 | 708 |
| YZS01-13 | 17.09 | 206.9 | 73.9 | 345.5 | 65.7 | 589.7 | 113.1 | 1522 | 94.90 | 0.33 | 1.502 | 0.004 | 723 |
| YZS01-14 | 23.72 | 262.7 | 85.9 | 392.4 | 75.2 | 660.5 | 123.0 | 1773 | 35.17 | 0.32 | 1.233 | 0.003 | 819 |
| YZS01-15 | 19.46 | 207.7 | 69.2 | 303.2 | 55.8 | 484.5 | 90.8 | 1356 | 20.08 | 0.42 | 1.982 | 0.001 | 757 |

**Appendix Table A3** *(continued)*

| Analyzed Spot | Tb | Dy | Ho | Er | Tm | Yb | Lu | ΣREE | Ce(IV)/Ce(III) | $Eu_N/Eu_N^*$ | $10000 \times (Eu_N/Eu_N^*)/Y$ | (Ce/Nd)/Y | T (°C)[2] |
|---|---|---|---|---|---|---|---|---|---|---|---|---|---|
| YZS01-18 | 12.54 | 157.8 | 59.3 | 289.1 | 57.7 | 532.4 | 105.0 | 1317 | 237.68 | 0.33 | 1.799 | 0.009 | 740 |
| YZS01-19 | 23.77 | 291.3 | 102.2 | 477.2 | 93.5 | 831.6 | 153.1 | 2117 | 95.09 | 0.29 | 0.938 | 0.003 | 760 |
| YZS01-20 | 17.20 | 208.4 | 72.7 | 343.7 | 67.7 | 604.7 | 113.1 | 1537 | 85.99 | 0.30 | 1.383 | 0.007 | 741 |
| YZS01-21 | 7.13 | 85.5 | 31.4 | 148.1 | 29.8 | 273.5 | 52.3 | 677 | 191.63 | 0.36 | 3.792 | 0.015 | 698 |
| YZS01-22 | 11.35 | 131.0 | 45.9 | 209.0 | 40.7 | 370.6 | 71.1 | 955 | 46.62 | 0.41 | 2.977 | 0.003 | 770 |
| YZS01-23 | 7.16 | 80.6 | 26.9 | 122.0 | 23.8 | 214.6 | 41.9 | 568 | 39.59 | 0.32 | 3.825 | 0.007 | 792 |
| YZS01-24 | 10.19 | 131.2 | 49.0 | 238.5 | 47.3 | 426.5 | 83.2 | 1030 | 62.33 | 0.25 | 1.661 | 0.008 | 701 |
| YZS01-25 | 17.29 | 216.6 | 80.4 | 390.1 | 76.9 | 707.0 | 137.1 | 1719 | 85.13 | 0.27 | 1.087 | 0.004 | 760 |
| YZS01-26 | 15.10 | 171.4 | 59.1 | 271.0 | 52.6 | 472.3 | 89.9 | 1239 | 45.51 | 0.40 | 2.200 | 0.003 | 764 |
| YZS01-28 | 16.43 | 189.4 | 64.9 | 295.8 | 56.3 | 500.9 | 93.6 | 1330 | 61.53 | 0.41 | 2.071 | 0.004 | 765 |
| YZS01-29 | 11.56 | 144.7 | 51.6 | 243.0 | 48.2 | 438.5 | 82.0 | 1110 | 59.74 | 0.29 | 1.824 | 0.011 | 713 |
| YZS01-30 | 12.96 | 145.0 | 49.3 | 227.6 | 43.9 | 399.2 | 79.2 | 1047 | 22.89 | 0.41 | 2.641 | 0.003 | 806 |
| *K-feldspar granite porphyry* | | | | | | | | | | | | | |
| YZS02-05 | 23.76 | 276.5 | 97.8 | 452.1 | 83.1 | 721.4 | 136.2 | 1921 | 38.22 | 0.02 | 0.056 | 0.001 | 761 |
| YZS02-07 | 8.45 | 105.5 | 38.7 | 187.5 | 36.1 | 325.5 | 61.6 | 814 | 153.17 | 0.01 | 0.092 | 0.010 | 719 |
| YZS02-15 | 29.28 | 335.5 | 114.0 | 525.3 | 94.4 | 818.9 | 152.1 | 2238 | 22.94 | 0.01 | 0.044 | 0.001 | 781 |
| YZS02-16 | 21.64 | 237.1 | 80.5 | 354.8 | 63.9 | 545.8 | 99.9 | 1557 | 24.34 | 0.01 | 0.057 | 0.002 | 816 |
| YZS02-27 | 6.90 | 83.0 | 30.6 | 148.0 | 28.4 | 255.5 | 50.2 | 647 | 24.04 | 0.06 | 0.645 | 0.009 | 802 |
| YZS02-29 | 4.07 | 51.0 | 19.7 | 103.1 | 22.6 | 236.9 | 51.5 | 521 | 53.81 | 0.32 | 4.791 | 0.019 | 763 |

| Reject data | Ce(IV)/Ce(III) | $Eu_N/Eu_N^*$ | $10000 \times (Eu_N/Eu_N^*)/Y$ | (Ce/Nd)/Y |
|---|---|---|---|---|
| *Granite porphyry* | | | | |
| YZS01-16 | 5.35 | 0.53 | 1.476 | 0.000 |
| YZS01-17 | 14.22 | 0.32 | 0.732 | 0.001 |
| YZS01-27 | 17.14 | 0.41 | 4.338 | 0.007 |
| *K-feldspar granite porphyry* | | | | |
| YZS02-01 | 3.43 | 0.02 | 0.078 | 0.001 |
| YZS02-02 | 7.04 | 0.01 | 0.048 | 0.002 |
| YZS02-03 | 4.90 | 0.01 | 0.088 | 0.002 |
| YZS02-04 | 2.83 | 0.02 | 0.060 | 0.001 |
| YZS02-06 | 1.07 | 0.06 | 0.221 | 0.001 |
| YZS02-08 | 1.85 | 0.04 | 0.144 | 0.001 |
| YZS02-09 | 2.52 | 0.01 | 0.053 | 0.001 |
| YZS02-10 | 4.00 | 0.03 | 0.082 | 0.001 |
| YZS02-11 | 4.27 | 0.03 | 0.133 | 0.001 |
| YZS02-12 | 8.80 | 0.01 | 0.082 | 0.003 |
| YZS02-13 | 3.95 | 0.01 | 0.060 | 0.002 |
| YZS02-14 | 2.39 | 0.02 | 0.055 | 0.001 |
| YZS02-17 | 3.12 | 0.01 | 0.095 | 0.002 |
| YZS02-18 | 3.86 | 0.01 | 0.025 | 0.001 |
| YZS02-19 | 7.55 | 0.01 | 0.098 | 0.003 |
| YZS02-20 | 4.71 | 0.15 | 0.657 | 0.001 |
| YZS02-21 | 8.83 | 0.02 | 0.123 | 0.003 |
| YZS02-22 | 3.71 | 0.04 | 0.114 | 0.001 |
| YZS02-23 | 7.43 | 0.06 | 0.618 | 0.005 |
| YZS02-24 | 6.61 | 0.03 | 0.028 | 0.000 |
| YZS02-25 | 2.01 | 0.01 | 0.039 | 0.001 |
| YZS02-26 | 3.89 | 0.01 | 0.092 | 0.002 |
| YZS02-28 | 2.89 | 0.03 | 0.249 | 0.002 |
| YZS02-30 | 7.59 | 0.08 | 0.172 | 0.000 |

[1] The analyses with Ca > 200 ppm or La > 0.3 ppm may reflect apatite contamination, and those data with Ti > 20 ppm may reflect titanite contamination, all of which have been omitted.

[2] Temperatures were calculated using the Ti-in-zircon thermometer (Ferry and Watson, 2007): log (ppm Ti-in-zircon) = (5.711 ± 0.072) − (4800 ± 86)/T (K) − log $a_{SiO2}$ + log $a_{TiO2}$, wherein $a_{SiO2}$ = 1 because of the existence of quartz, and $a_{TiO2}$ = 0.6 due to the present of the titanite.

## References


Ballard, J.R., Palin, J.M., Campbell, I.H., 2002. Relative oxidation states of magmas inferred from Ce(IV)/Ce(III) in zircon: application to porphyry copper deposits of northern Chile. Contrib. Miner. Petrol. 144 (3), 347–364.

Burnham, C.W., 1979. Magmas and hydrothermal fluids. In: Barnes, H.L. (Ed.), Geochemistry of Hydrothermal Ore Deposits, second ed. John Wiley and Sons, New York, pp. 71–136.

Candela, P.A., Piccoli, P.M., 2005. Magmatic processes in the development of porphyry-type ore systems. In: In: Hedenquist, J.W., Thompson, J.F.H., Goldfarb, R.J., Richards, J.P. (Eds.), Economic Geology 100. pp. 25–38.

Candela, P.A., 1992. Controls on ore metal ratios in granite-related ore systems: an experimental and computational approach. Trans. R. Soc. Edinburgh Earth Sci. 83, 317–326.

Chappell, B., White, A., 2001. Two contrasting granite types: 25 years later. Aust. J. Earth Sci. 48, 489–499.

Chambefort, I., Dilles, J.H., Kent, A.J.R., 2008. Anhydrite-bearing andesite and dacite as a source for sulfur in magmatic-hydrothermal mineral deposits. Geology 36, 719–722.

Chiaradia, M., Ulianov, A., Kouzmanov, K., Beate, B., 2012. Why large porphyry Cu deposits like high Sr/Y magmas? Sci. Rep. 2, 685.

Claiborne, L.L., Miller, C.F., Wooden, J.L., 2010. Trace element composition of igneous zircon: a thermal and compositional record of the accumulation and evolution of a large silicic batholith, Spirit Mountain, Nevada. Contrib. Miner. Petrol. 160, 511–531.

Cline, J.S., Bodnar, R.J., 1991. Can economic porphyry copper mineralization be generated by a typical calc-alkaline melt? J. Geophys. Res. Solid Earth 96 (B5), 8113–8126.

Dilles, J.H., Kent, A.J.R., Wooden, J.L., Tosdal, R.M., Koleszar, A., Lee, R.G., Farmer, L.P., 2015. Zircon compositional evidence for sulfur-degassing from ore-forming arc magmas. Econ. Geol. 110 (1), 241–251.

Ding, X., Jiang, S.Y., Ni, P., Gu, L.X., Jiang, Y.H., 2005. Zircon SIMS U-Pb geochronology of host granitoids in Wushan and Yongping copper deposits, Jiangxi Province. Geol. J. China Univ. 11 (3), 383–389 (in Chinese).

Dostal, J., Capedri, S., 1978. Uranium in metamorphic rocks. Contrib. Miner. Petrol. 66, 409–414.

El Bouseilly, A.M., El Sokkary, A.A., 1975. The relation between Rb, Ba, and Sr in granitic rocks. Chem. Geol. 16 (1975), 207–219.

Feng, C.Y., Zhang, D.Q., Xiang, X.K., Li, D.X., Qu, H.Y., Liu, J.N., Xiao, H., 2012. Re-Os isotopic dating of molybdenite from the Dahutang tungsten deposit in northwestern Jiangxi Province and its geological implication. Acta Petrol. Sin. 28 (12), 3858–3868 (in Chinese).

Ferry, J.M., Watson, E.B., 2007. New thermodynamic models and revised calibrationsfor the Ti-in-zircon and Zr-in-rutile thermometers. Contrib. Mineral. Petrol. 154 (4), 429–437. https://doi.org/10.1007/s00410-007-0201-0.

Fletcher, C.J.N., Chan, L.S., Sewell, R.J., Diarmad, S., Campbell, G., Davis, D.W., Zhu, J., 2004. Basement Heterogeneity in the Cathaysia Crustal Block, southeast China Aspects of the Tectonic Evolution of China. Geological Society of London.

Förster, H.J., Tischendorf, G., Trumbull, R.B., Gottesmann, B., 1999. Late-collisional granites in the Variscan Erzgebirge, Germany. J. Petrol. 40, 1613–1645.

Griffin, W.L., Begg, G.C., O'Reilly, S.Y., 2013. Continental-root control on the genesis of magmatic ore deposits. Nat. Geosci. 6 (11), 905–910.

Guo, C.L., Chen, Y.C., Li, C.B., et al., 2011. Zircon SHRIMP U-Pb dating, geochemistry, Sr-Nd isotopic analysis of the Late Jurassic granitoids in the Jiulongnao W-Sn-Pb-Zn ore-concentrated areas in Jiangxi province and their geological significance. Acta Geol. Sin. 85, 1188–1205 (in Chinese).

Hall, A., Jarvis, K., Walsh, J., 1993. The variation of cesium and 37 other elements in the Sardinian granite batholith, and the significance of cesium for granite petrogenesis. Contrib. Miner. Petrol. 114, 160–170.

Halter, W.E., Heinrich, C.A., Pettke, T., 2005. Magma evolution and the formation of porphyry Cu–Au ore fluids: evidence from silicate and sulfide melt inclusions. Miner. Deposita 39, 845–863.

Hart, S.R., 1984. A large-scale isotope anomaly in the Southern Hemisphere mantle. Nature 309 (5971), 753–757.

Hedenquist, J.W., Lowenstern, J.B., 1994. The role of magmas in the formation of hydrothermal ore deposits. Nature 370, 519–527.

Hoskin, P.W.O., Schaltegger, U., 2003. The composition of zircon and igneous and metamorphic petrogenesis. Rev. Mineral. Geochem. 53, 27–62.

Hou, Z., Zhou, Y., Wang, R., Zheng, Y., He, W., Zhao, M., Evans, N.J., Weinberg, R.F., 2017. Recycling of metal-fertilized lower continental crust: Origin of non-arc Au-rich porphyry deposits at cratonic edges. Geology 45 (6), 563–566.

Hou, Z., Yang, Z., Lu, Y., Kemp, A., Zheng, Y., Li, Q., Tang, J., Yang, Z., Duan, L., 2015. A genetic linkage between subduction- and collision-related porphyry Cu deposits in continental collision zones. Geology 43 (3), 247–250.

Huang, L.C., Jiang, S.Y., 2014. Highly fractionated S-type granites from the giant Dahutang tungsten deposit in Jiangnan Orogen, Southeast China: geochronology, petrogenesis and their relationship with W-mineralization. Lithos 202–203, 207–226.

Jiang, Y.H., Jiang, S.Y., Zhao, K.D., Ling, H.F., 2006. Petrogenesis of Late Jurassic Qianlishan granites and mafic dikes, southeast China: implications for a back-arc extension setting. Geol. Mag. 143, 457–474.

Jugo, P.J., 2009. Sulfur content at sulfide saturation in oxidized magmas. Geology 37, 415–418.

JXBGMR (Bureau of Geology and Mineral Resources of Jiangxi Province), 1984. Regional Geology of the Jiangxi Province. Geological Publishing House, Beijing, pp. 1–921 (in Chinese with English abstract).

JXBGMR (Department of Geology and Mineral Resources of Jiangxi Province), 1997. Stratigraphy (Lithostratic) of Jiangxi Province. China University of Geosciences Press, Wuhan, pp. 9–50 (in Chinese).

Kemp, A.I.S., Blevin, P., Whitehouse, M., EIMF, 2011. Forensic zirconology: tracing the magmatic and metallogenic evolution of intrusive porphyries of the Macquarie Arc, NSW, Australia. In: 11th SGA Biennial Meeting, Let's Talk Ore Deposits, 26–29th September 2011 Antofagasta, Chile, pp. 429–431.

Leng, C.B., Qi, Y.Q., 2018. The Genesis of Lengshuikeng Ag-Pb-Zn Orefield: Constrains from in-situ LA-ICPMS Analyses of Minor and Trace Elements for Sphalerite and Galena. Acta Geol. Sin. 91 (10), 2256–2272 (in Chinese).

Li, J.H., Zhang, Y.Q., Dong, S.W., Johnston, S.T., 2014. Cretaceous tectonic evolution of South China: a preliminary synthesis. Earth Sci. Rev. 134, 98–136.

Li, L.M., Sun, M., Wang, Y.J., Zhao, G.C., Lin, S.F., Xi, X.P., Chan, L.S., Zhang, F.F., Wong, J., 2011. U-Pb and Hf isotopic study of zircons from migmatised amphibolites in the Cathaysia Block: Implications for the early Paleozoic peak tectonothermal event in southeastern China. Gondwana Res. 19, 191–201.

Li, W.X., Li, X.H., Li, Z.X., Lou, F.S., 2008. Obduction-type granites within the NE Jiangxi Ophiolite: implications for the final amalgamation between the Yangtze and Cathaysia Blocks. Gondwana Res. 13, 288–301.

Li, X.F., Watanabe, Y., Qu, W.J., 2007. Textures and geochemical characteristics of granitic rocks in the Yongping climaxtype Cu-Mo deposit, Jiangxi, southeastern China, and their alteration, mineralization and tectonic regime. Acta Petrol. Sin. 23 (10), 2353–2365 (in Chinese).

Li, X.H., Liu, Y., Li, Q.L., Guo, C.H., Chamberlain, K.R., 2009. Precise determination of Phanerozoic zircon Pb/Pb age by multicollector SIMS without external standardization. Geochem. Geophys. Geosyst. 10, Q04010.

Li, X.H., Long, W.G., Li, Q.L., Liu, Y., Zheng, Y.F., Yang, Y.H., Chamberlain, K.R., Wan, D.F., Guo, C.H., Li, X., Tang, G., Gong, B., Yang, Y., Hou, K., Hu, Z., Li, Q., Liu, Y., Li, W., 2013a. Qinghu zircon: a working reference for microbeam analysis of U-Pb age and Hf and O isotopes. Chin. Sci. Bull. 58, 4647–4654.

Li, Z.L., Zhou, J., Mao, J.R., Santosh, M., Yu, M.G., Li, Y.Q., Hu, Y.Z., Langmuir, C.H., Chen, Z.X., Cai, X.X., Hu, Y.H., 2013b. Zircon U-Pb geochronology and geochemistry of two episodes of granitoids from the northwestern Zhejiang Province, SE China: implication for magmatic evolution and tectonic transition. Lithos 179, 334–352.

Li, Z.X., Li, X.H., Wartho, J.A., Clark, C., Li, W.X., Zhang, C.L., Bao, C., 2010. Magmatic andmetamorphic events during the Early PaleozoicWuyi-Yunkai Orogeny, southeastern South China: new age constraints and P-T conditions. Geol. Soc. Am. Bull. 122, 772–793.

Liang, H.-Y., Campbell, I.H., Allen, C., Sun, W.-D., Liu, C.-Q., Yu, H.-X., Xie, Y.-W., Zhang, Y.-Q., 2006. Zircon Ce4+/Ce3+ ratios and ages for Yulong ore-bearing porphyries in eastern Tibet. Miner. Deposita 41, 152–159.

Ling, H.F., Xu, S.J., Shen, W.Z., Wang, R.C., Lin, Y.P., 1998. Nd, Sr, Pb and O isotopic compositions of Late Proterozoic Gezong- and Donggu-granites in the west margin of Yangtze plate and comparison with other coeval granitoids. Acta Petrol. Sin. 14, 269–277 (in Chinese).

Liu, X., Sun, Z.M., Ma, Y.S., 1994. Ore-controlling Structure and Ore-forming Prediction in North Wuyishan and Surrounding Area. Seismological Publishing House, Beijing, pp. 1–192 (in Chinese).

Liu, Y.S., Gao, S., Hu, Z.C., Gao, C.G., Zong, K.Q., Wang, D.B., 2010. Continental and Oceanic Crust Recycling-induced Melt-Peridotite Interactions in the Trans-North China Orogen: U-Pb Dating, Hf Isotopes and Trace Elements in Zircons from Mantle Xenoliths. J. Petrol. 51 (1–2), 537–571.

Loader, M.A., Wilkinson, J.J., Armstrong, R.N., 2017. The effect of titanite crystallisation on Eu and Ce anomalies in zircon and its implications for the assessment of porphyry Cu deposit fertility. Earth Planet. Sci. Lett. 472, 107–119.

Loucks, R.R., 2014. Distinctive composition of copper-ore-forming arc magmas. Aust. J. Earth Sci. 61, 5–16.

Lu, H.J., Hua, R.M., Mao, G.Z., Long, G.M., 2007. Isotope geochronological study of igneous rocks in Northeastern Jiangxi Province and its implication to geologic evolution. Geol. Rev. 53, 207–216 in Chinese.

Lu, R., Mao, J.W., Gao, J.J., Su, H.M., Zheng, J.H., 2012. Geological characteristics and occurrence of silver in Xiabao Ag-Pb-Zn Deposit, Lengshuikeng Ore Field, Jiangxi Province, East China. Acta Petrol. Sin. 28 (1), 105–121 (in Chinese).

Lu, Y.J., Loucks, R.R., Fiorentini, M.L., Yang, Z.-M., Hou, Z.-Q., 2015. Fluid flux melting generated post-collisional high Sr/Y copper ore-forming water-rich magmas in Tibet. Geology 43, 583–586.

Lu, Y.J., Loucks, R.R., Fiorentini, M., McCuaig, T.C., Evans, N.J., Yang, Z.M., Hou, Z.Q., Kirkland, C.L., Parra-Avila, L.A., Kobussen, A., 2016. Zircon compositions as a pathfinder for porphyry Cu ± Mo ± Au deposits. Soc. Econ. Geol. Spec. Publ. 19, 329–347.

Ludwig, K.R., 2008. User's Manual for Isoplot 3.70: a Geochronological Toolkit for Microsoft Excel. Kenneth R. Ludwig.

Luo, P., Wu, G.G., Zhang, D., Di, Y.J., Wang, C.M., Wang, Y.Q., 2009. Geochemistry and genesis of Shengmikeng lead-zinc deposit in northern Wuyi, Eastern China. J. Geomech. 15 (4), 349–362 (in Chinese).

Ma, L.Y., Lu, Y.F., Mei, Y.P., Chen, X.Q., 2006. Zircon SHRIMP U-Pb dating of granodiorite from Shuikoushan ore-field, Hunan Province and its geological significance. Acta Petrol. Sin. 22, 2475–2482 (in Chinese).

Mao, J.W., Xie, G.Q., Guo, C.L., Chen, Y.C., 2007. Large-scale tungsten-tin mineralization in the Nanling region, South China: metallogenic ages and corresponding geodynamic process. Acta Petrol. Sin. 23 (10), 2329–2338 (in Chinese).

Megaw, P.K., Ruiz, J., Titley, S.R., 1988. High-temperature, carbonate-hosted Ag-Pb-Zn (Cu) deposits of northern Mexico. Econ. Geol. 83 (8), 1856–1885.

Mei, Y.W., 1998. The Wuyishan orogen and its ore-forming process. Jiangxi Geol. 12, 109–115 (in Chinese).

Meng, X.J., Hou, Z.Q., Dong, G.Y., Liu, J.G., Qu, W.J., Yang, Z.S., Zuo, L.Y., Xiao, M.Z., 2007. The geological characteristics and Re-Os isotope age of molybdenite of the Xiongjiashan molybdenum deposit, Jiangxi Province. Acta Geol. Sin. 81 (7), 946–951

(in Chinese).
Meng, X.J., Xu, W.Y., Yang, Z.S., Hou, Z.Q., Li, Z.Q., Yu, Y.S., Xiao, M.Z., He, X.R., Wan, H.Z., 2012. Time limit of volcanic-magmatic action in Lengshuikeng orefield, Jiangxi: evidence from SHRIMP zircon U-Pb ages. Mineral Deposits 31 (4), 831–838 (in Chinese).
Moore, G., Carmichael, I., 1998. The hydrous phase equilibria (to 3 kbars) of an andesite and basaltic andesite from western Mexico: constraints on water content and conditions of phenocryst growth. Contrib. Miner. Petrol. 130, 304–319.
Mungall, J.E., 2002. Roasting the mantle: Slab melting and the genesis of major Au and Au-rich Cu deposits. Geology 30 (10), 915–918.
Patiño Douce, A.E., 1999. What do experiments tell us about the relative contributions of crust and mantle to the origin of granitic magmas? Geol. Soc. Lond. Spec. Publ. 168, 55–75.
Pearce, J.A., Thirlwall, M.F., Ingram, G., Murton, B.J., Arculus, R.J., Vander Laan, S.R., 1992. Isotopic evidence for the origin of Boninites and related rocks drilled in the Izu–Bonin (Ogasawara) forearc, Leg 125. In: In: Fryer, P., Pearce, J.A., Stokking, L. (Eds.), Proceedings of the Ocean Drilling Program. Scientific Results 125. pp. 237–261.
Qi, L., Hu, J., Gregoire, D.C., 2000. Determination of trace elements in granites by inductively coupled plasma mass spectrometry. Talanta 51 (3), 507–513.
Qi, Y.Q., Hu, R.Z., Li, X.F., Leng, C.B., Liu, S., Wu, L.Y., Liu, R., 2015. Mineral chemical characteristics of sphalerite and genetic constraints of iron and manganese carbonate in Lengshuikeng Ag-Pb-Zn ore deposit, Jiangxi Province, China. Acta Mineral. Sin. 35 (2), 136–146 (in Chinese).
Qi, Y.Q., Hu, R.Z., Liu, S., Coulson, I.M., Qi, H.W., Tian, J.J., Feng, C.X., Wang, T., 2012. Geochemical and Sr-Nd-Pb isotopic compositions of Mesozoic mafic dikes from the Gan-Hang tectonic belt, South China: petrogenesis and geodynamic significance. Int. Geol. Rev. 54 (8), 920–939.
Qi, Y.Q., Hu, R.Z., Liu, S., Coulson, I.M., Qi, H.W., Tian, J.J., Zhu, J.J., 2016. Petrogenesis and geodynamic setting of Early Cretaceous mafic-ultramafic intrusions, South China: A case study from the Gan-Hang tectonic belt. Lithos 258–259, 149–162.
Qin, S.T., 2011. Petrological characteristics of the Lidongshan PD1 profile in Huangbi Mine district, Yanshan County, Jiangxi Province. Master Thesis. China University of Geosciences, Beijing, pp. 1–99 (in Chinese).
Qiu, J.S., Yang, Z.L., Xing, G.F., Yu, M.G., Zhao, J.L., wang, R.Q., 2015. A comparison study between Caledonian and Yanshanian granites from Xiongjiashan molybdenum deposit in Jinxi County, Jiangxi Province, and its implications to metallogenesis. Acta Petrol. Sin. 31 (3), 656–674.
Qiu, J.T., Yu, X.Q., Wu, G.G., Liu, J.G., Xiao, M.Z., 2013. Geochronology of igneous rocks and nappe structures in Lengshuikeng deposit, Jiangxi Province, China. Acta Petrol. Sin. 29 (3), 812–826 (in Chinese).
Richards, J.P., 2003. Tectono-magmatic precursors for porphyry Cu-(Mo-Au) deposit formation. Econ. Geol. Bull. Soc. Econ. Geol. 98 (8), 1515–1533.
Richards, J.P., Kerrich, R., 2007. Special Paper: Adakite-like rocks: Their diverse origins and questionable role in metallogenesis. Econ. Geol. 102, 537–576.
Richards, J.P., 2009. Postsubduction porphyry Cu-Au and epithermal Au deposits: products of remelting of subduction-modified lithosphere. Geology 37 (3), 247–250.
Richards, J.P., 2011. High Sr/Y arc magmas and porphyry Cu ± Mo ± Au deposits: just add water. Econ. Geol. 106, 1075–1081.
Simmons, S.F., White, N.C., John, D.A., 2005. Geological characteristics of epithermal precious and base metal deposits. In: Hedenquist, J.W., Thompson, J.F.H., Goldfarb, R.J., Richards, J.P. (Eds.), Economic Geology One Hundredth Anniversary Volume: 1905–2005. Society of Economic Geologists Littleton, CO, U.S.A., pp. 485–522.
Sláma, J., Košler, J., Condon, D.J., Crowley, J.L., Gerdes, A., Hanchar, J.M., Horstwood, M.S., Morris, G.A., Nasdala, L., Norberg, N., 2008. Plešovice zircon—a new natural reference material for U-Pb and Hf isotopic microanalysis. Chem. Geol. 249, 1–35.
Streck, M.J., Dilles, J.H., 1998. Sulfur evolution of oxidized arc magmas as recorded in apatite from a porphyry copper batholith. Geology 26, 523–526.
Su, H.M., Mao, J.W., He, X.R., Lu, R., 2013. Timing of the formation of the Tianhuashan Basin in northern Wuyi as constrained by geochronology of volcanic and plutonic rocks. Sci. China Earth Sci. 56, 940–955.
Su, H.M., Mao, J.W., Santosh, M., Xie, G.Q., 2014. Petrogenesis and tectonic significance of Late Jurassic-Early Cretaceous volcanic-intrusive complex in the Tianhuashan basin, South China. Ore Geol. Rev. 56, 566–583.
Su, H.M., Zhang, C.S., 2012. U-Pb ages and Hf isotopes of detrital zircons of mica quartz schist from the Guixi area in northeastern Jiangxi Province and its geological significance. Geol. China 39, 1577–1592.
Sun, W., Wang, J., Zhang, L., Zhang, C., Li, H., Ling, M., Ding, X., Li, C., Liang, H., 2017. The formation of porphyry copper deposits. Acta Geochim. 36 (1), 9–15.
Sun, S.S., McDonough, W.F., 1989. Chemical and isotopic systematics of oceanic basalts: implications for mantle composition and processes. Geol. Soc., Lond., Spec. Publ. 42 (1), 313–345.
Trail, D., Watson, E.B., Tailby, N.D., 2011. The oxidation state of Hadean magmas and implications for early Earth's atmosphere. Nature 480, 79–82.
Trail, D., Watson, E.B., Tailby, N.D., 2012. Ce and Eu anomalies in zircon as proxies for the oxidation state of magmas. Geochim. Cosmochim. Acta 97, 70–87.
Wang, C.M., Wu, G.G., Zhang, D., Luo, P., Di, Y.J., Yu, X.Q., 2010. Regional metallogenic characteristics and mineralizing pedigree in northeastern Jiangxi. Global Geol. 29, 588–600 (in Chinese).
Wang, C.M., Zhang, D.A., Wu, G.G., Xu, Y.G., Carranza, E.J.M., Zhang, Y.Y., Li, H.K., Geng, J.Z., 2013a. Zircon U-Pb geochronology and geochemistry of rhyolitic tuff, granite porphyry and syenogranite in the Lengshuikeng ore district, SE China: Implications for a continental arc to intra-arc rift setting. J. Earth Syst. Sci. 122, 809–830.
Wang, C.M., Zhang, D.A., Wu, G.G., Santosh, M., Zhang, J., Xu, Y.G., Zhang, Y.Y., 2014a. Geological and isotopic evidence for magmatic-hydrothermal origin of the Ag–Pb–Zn deposits in the Lengshuikeng District, east-central China. Miner. Deposita 49 (6), 733–749.
Wang, D.Z., Liu, C.S., Shen, W.Z., Chen, F.R., 1993. The contrast between Tonglu I-type and Xiangshan S-type clasto-porphyritic lava. Acta Petrol. Sin. 9 (1), 44–53 (in Chinese).
Wang, R., Richards, J.P., Hou, Z., Yang, Z., DuFrane, S.A., 2014b. Increased magmatic water content—the key to Oligo-Miocene porphyry Cu-Mo ± Au formation in the eastern Gangdese belt, Tibet. Econ. Geol. 109, 1315–1339.
Wang, R., Richards, J.P., Hou, Z.-Q., Yang, Z.-M., Gou, Z.-B., DuFrane, S.A., 2014c. Increasing magmatic oxidation state from Paleocene to Miocene in the eastern Gangdese belt, Tibet: Implication for collision-related porphyry Cu-Mo ± Au mineralization. Econ. Geol. 109, 1943–1965.
Wang, Y.J., Fan, W.M., Zhang, G.W., Zhang, Y.H., 2013b. Phanerozoic tectonics of the South China Block: key observations and controversies. Gondwana Res. 23, 1273–1305.
Wiedenbeck, M., Alle, P., Corfu, F., Griffin, W., Meier, M., Oberli, F., Quadt, A.V., Roddick, J., Spiegel, W., 1995. Three natural zircon standards for U-Th-Pb, Lu-Hf, trace element and REE analyses. Geostand. Newslett. 19, 1–23.
Williams-Jones, A.E., Heinrich, C.A., 2005. 100th anniversary special paper: vapor transport of metals and the formation of magmatic-hydrothermal ore deposits. Econ. Geol. 100 (7), 1287–1312.
Winchester, J.A., Floyd, P.A., 1977. Geochemical discrimination of different magma series and their differentiation products using immobile elements. Chem. Geol. 20, 325–343.
Wong, J., Sun, M., Xing, G.F., Zhao, G.C., Wong, K., Wu, F.Y., 2011. Zircon U-Pb and Hf isotopic study of Mesozoic felsic rocks from eastern Zhejiang, South China: geochemical contrast between the Yangtze and Cathaysia blocks. Gondwana Res. 19, 244–259.
Wu, F.Y., Ji, W.Q., Sun, D.H., Yang, Y.H., Li, X.H., 2012. Zircon U-Pb geochronology and Hf isotopic compositions of the Mesozoic granites in southern Anhui Province, China. Lithos 150, 6–25.
Wu, F.Y., Sun, D.Y., Li, H.M., Jahn, B.M., Wilde, S., 2002. A-type granites in northeastern China: age and geochemical constraints on their petrogenesis. Chem. Geol. 187 (1–2), 143–173.
Xie, D.Q., Li, K.D., Xu, Q.S., Luo, P., 2006. The prospecting orentation and target area selective preference of metallic deposits in the north of Wuyi Mountain. J. East China Instit. Technol., Suppl. 24–27 (in Chinese).
Xie, J.C., Yang, X.Y., Sun, W.D., Du, J.G., 2012. Early Cretaceous dioritic rocks in the Tongling region, eastern China: implications for the tectonic settings. Lithos 150, 49–61. https://doi.org/10.1016/j.lithos.2012.05.008.
Xu, L., Bi, X., Hu, R., Qi, Y., Tang, Y., Wang, X., Zhu, J., 2016. Redox states and genesis of magmas associated with intra-continental porphyry Cu–Au mineralization within the Jinshajiang-Red River alkaline igneous belt, SW China. Ore Geol. Rev. 73 (Pt. 2), 330–345.
Yang, M.G., Wang, F.N., Zeng, Y., Lai, X.P., Huang, S.B., Zhou, H., 2004. Metallogenic Geology in the North Part of Jiangxi Province. China Land Press, Beijing 1–186 (in Chinese).
Yang, S.Y., Jiang, S.Y., Zhao, K.D., Jiang, Y.H., Ling, H.F., Luo, L., 2012. Geochronology, geochemistry and tectonic significance of two Early Cretaceous A-type granites in the Gan-Hang Belt, Southeast China. Lithos 150, 155–170.
Yao, J.M., Hua, R.M., Lin, J.F., 2005. Zircon LA-ICPMS U-Pb dating and geochemical characteristics of Huangshaping granite in southeast Hunan province, China. Acta Petrol. Sin. 21, 688–696 (in Chinese).
Yao, J.M., Hua, R.M., Qu, W.J., Qi, H.W., Lin, J.F., Du, A.D., 2007. Re-Os isotope dating of molybdenites in the Huangshaping Pb-Zn-W-Mo polymetallic deposit, Hunan province, South China and its geological significance. Sci. China Earth Sci. 50, 519–526.
Yardley, B.W.D., Valley, J.W., 1997. The petrologic case for a dry lower crust. J. Geophys. Res.—Solid Earth 102, 12173–12185.
Ye, Q.T., 1987. Metallogenetic series of lead-zinc ore deposits in Northeast Jiangxi. Beijing Science and Technology Press, Beijing, pp. 1–104 (in Chinese).
Yu, J.H., Wang, L.J., O'Reilly, S.Y., Griffin, W.L., Zhang, M., Li, C.Z., Shu, L.S., 2009. A Paleoproterozoic orogeny recorded in a long-lived cratonic remnant (Wuyishan terrane), eastern Cathaysia Block, China. Precambrian Res. 174, 347–363.
Yu, X.Q., Wu, G.G., Zhao, X.X., Zhang, D., Di, Y.J., Qiu, J.T., Dai, Y.P., Li, C.L., 2012. New geochronological data from the Paleozoic and Mesozoic nappe structures, igneous rocks, and molybdenite in the North Wuyi area, Southeast China. Gondwana Res. 22 (2), 519–533.
Yuan, S.D., Peng, J.T., Hu, R.Z., Li, H.M., Shen, N.P., Zhang, D.L., 2008. A precise U-Pb age on cassiterite from the Xianghualing tin-polymetallic deposit (Hunan, South China). Miner. Deposita 43 (4), 375–382.
Yuan, S.D., Peng, J.T., Hao, S., Li, H.M., Geng, J.Z., Zhang, D.L., 2011. In situ LA-MC-ICP-MS and ID-TIMS U-Pb geochronology of cassiterite in the giant Furong tin deposit, Hunan Province, South China: New constraints on the timing of tin-polymetallic mineralization. Ore Geol. Rev. 43, 235–242.
Yuan, S.D., Williams-Jones, A.E., Mao, J.W., Zhao, P.L., Yan, C., Zhang, D.L., 2018. The origin of the Zhangjialong tungsten deposit, South China: Implications for W-Sn mineralization in large granite batholiths. Econ. Geol. 113 (5), 1193–1208.
Yuan, S.D., Williams-Jones, A.E., Romer, R.L., Zhao, P.L., Mao, J.W., 2019. Protolith-related thermal controls on the decoupling of Sn and W in Sn-W metallogenic provinces: Insights from the Nanling region, China. Econ. Geol. 114, 1005–1012.
Zajacz, Z., Halter, W.E., Pettke, T., Guillong, M., 2008. Determination of fluid/melt partition coefficients by LA-ICPMS analysis of co-existing fluid and silicate melt inclusions: Controls on element partitioning. Geochim. Cosmochim. Acta 72 (8), 2169–2197.
Zhang, H., Ling, M.X., Liu, Y.L., Tu, X.L., Wang, F.Y., Li, C.Y., Liang, H.Y., Yang, X.Y., Arndt, N.T., Sun, W.D., 2013. High oxygen fugacity and slab melting linked to Cu

mineralization: evidence from Dexing porphyry copper deposits, Southeastern China. J. Geol. 121, 289–305.
Zhang, J.J., Wu, M.S., Chen, Z.H., Liu, S.B., Li, L.X., Qiu, L.M., Wu, B., Huang, A.J., Zhu, P.J., 2009. Geochronologic study on the Jinzhuping molybdenum-polymetallic deposit from Shangrao of Jiangxi Province. Rock Miner. Anal. 28 (3), 228–232 (in Chinese).
Zhang, R.Q., Lu, J.J., Wang, R.C., et al., 2011. The confirmation of Yanshanian Biotite Granite in the Hehuaping Sn-Pb-Zn District, Southern Hunan Province, China. Geol. J. China Univ. 17, 513–520 (in Chinese).
Zhao, F.Q., 1999. The chronotectonic framework of basements from Cathaysia Block. Progr. Precambrian Res. 22 (2), 39–46.
Zhou, J.X., 1999. Geochemistry and Petrogenesis of Igneous Rocks Containing Amphibole and Mica: A Case Study of Plate Collision Involving Scotland and Himalayas. Science Press, New York and Beijing, pp. 41–72.
Zhou, T.F., Fan, Y., Yuan, F., Zhong, G.X., 2012. Progress of geological study in the Middle-Lower Yangtze River Valley metallogenic belt. Acta Petrol. Sin. 28 (10), 3051–3066 (in Chinese).
Zhu, J.J., Richards, J.P., Rees, C., Creaser, R., DuFrane, S.A., Locock, A., Petrus, J.A., Lang, J., 2018. Elevated magmatic sulfur and chlorine contents in ore-forming magmas at the red chris porphyry Cu-Au deposit, Northern British Columbia, Canada. Econ. Geol. 113, 1047–1075.
Zindler, A., Hart, S., 1986. Chemical geodynamics. Annu. Rev. Earth Planet. Sci. 14 (1), 493–571.
Zou, H.B., Zindler, A., Xu, X.S., Qi, Q., 2000. Major, trace element, and Nd, Sr and Pb isotope studies of Cenozoic basalts in SE China: mantle sources, regional variations, and tectonic significance. Chem. Geol. 171 (1–2), 33–47.
Zuo, L.Y., Hou, Z.Q., Meng, X.J., Yang, Z.M., Song, Y.C., Li, Z., 2010. SHRIMP U-Pb zircon geochronology of the ore-bearing rock in the Lengshuikeng porphyry type Ag–Pb–Zn deposit. Geol. China 37, 1450–1456 (in Chinese).